Mesoscopic structure of mixed type domain walls in multiaxial ferroelectrics

Anna N. Morozovska,[1,*] Eugene A. Eliseev,[2,†] Yevhen M. Fomichov,[3] and Sergei V. Kalinin[4,‡]

[1]*Institute of Physics, National Academy of Sciences of Ukraine, 46 prospect Nauky, 03028 Kyiv, Ukraine*

[2]*Institute for Problems of Materials Science, National Academy of Sciences of Ukraine, Krjijanovskogo 3, 03142 Kyiv, Ukraine*

[3]*Charles University in Prague, Faculty of Mathematics and Physics, V Holešovičkach 2, Prague 8, 180 00, Czech Republic*

[4]*The Center for Nanophase Materials Sciences, Oak Ridge National Laboratory, Oak Ridge, Tennessee 37922, USA*

(Received 12 August 2020; revised 20 October 2020; accepted 29 October 2020; published 13 November 2020)

The structure of a 180 ° uncharged rotational domain wall in a multiaxial ferroelectric film is studied in the framework of an analytical Landau-Ginzburg-Devonshire (LGD) approach. Finite element modeling (FEM) is used to solve numerically the system of the coupled nonlinear Euler-Lagrange (EL) second-order differential equations for two components of polarization. We show that the structure of the domain wall and corresponding metastable or stable phase of the film are controlled by a single parameter—the dimensionless ferroelectric anisotropy factor μ. We fitted the static profile of a solitary domain wall, calculated by FEM, with kinklike functions for polarization components, and extracted the five μ-dependent parameters from the fitting to FEM curves. The surprisingly high accuracy of the fitting results for two polarization components in the entire μ range allows us to conclude that the analytical functions, which are trial functions in the direct variational method, can be treated as a high-accuracy variational solution of the static EL equations. We further derive exact two-component analytical solutions of the static EL equations for a polydomain 180 ° domain structure in a multiaxial ferroelectric film. Using these, we derive analytical expressions for the system free energy and analyze its dependence on the film thickness and boundary conditions at the film surfaces. The single-domain state is ground for zero polarization derivative at the surfaces, while the polydomain states minimize the system energy for zero polarization at the surfaces. Counterintuitively, the energy of the polydomain states split into two levels, "0" and "1," for zero polarization at the surfaces, and each of the levels contains a large number of close-energy sublevels, whose structure is characterized by a different number and type of domain walls. The analytical solutions can become a useful tool for Bayesian analysis of high-resolution scanning transmission electron microscopy images in ferroelectric films.

DOI: 10.1103/PhysRevMaterials.4.114410

I. INTRODUCTION

Multiaxial ferroelectrics are one of the most fascinating representatives of materials with multiple interacting order parameters and key objects for fundamental exploration of nonlinear and cooperative phenomena at micro, nano, and atomic scales [1–4]. These materials undergo a temperature-driven phase transition accompanied by the appearance of a spontaneous polarization vector [5,6]. The spatial distribution of the spontaneous polarization is often characterized by a complex morphology of domain structure [7–10] and its nontrivial temporal evolution [11,12]. This interest is further stimulated by multiple applications in extant and emerging technologies in industrial, medical, and consumer sectors, including transducers, filters, sensors, ultrasonic motors and actuators, electronics, and information storage [13,14].

Theoretical modeling and practical control of the domain structure in multiaxial ferroelectrics is interesting from the fundamental viewpoint and also is important for many applications [5,6,15–20], but it is strongly complicated due to a wide range of contributing physical processes [21]. These involve interaction of domain walls with lattice potential barriers [22], point and planar defects [23–25] including charged acceptor/donor impurities and vacancies [26,27], electric and elastic dipolar defects [28–30], twin and grain boundaries [31], as well as screening conditions at surfaces and interfaces [32,33]. In ferroelectric thin films and their multilayers, which are intriguing objects of fundamental research and promising materials for nanoelectronics, decreasing the thickness usually leads to the ferroelectricity suppression and critically influences on the domain structure dynamics [34–36].

Seminal theoretical studies devoted to the structure of mixed Ising-Bloch-type [37,38] and Ising-Bloch-Néel-type [39,40] rotational domain walls in multiaxial ferroelectrics have been performed using the continuum Landau-Ginzburg-Devonshire (LGD) theory [41,42] implemented to the finite element modeling (FEM) or phase-field algorithms [18]. The approach allows obtaining accurate numerical results. However, due to the very complex nature of the above-mentioned phenomena, the analytical theory of domain structure thermodynamics and kinetics is in multiaxial ferroelectrics thin films is studied only weakly, with exceptions for several special cases [43–45]. Partially this dearth of studies has been

*Corresponding author: anna.n.morozovska@gmail.com

†Corresponding author: eugene.a.eliseev@gmail.com

‡Corresponding author: sergei2@ornl.gov

related to the lack, until recently, of direct information on domain-wall structure.

Recently, the emergence of the high-resolution scanning transmission electron microscopy (HR STEM) has allowed direct insight into the structure of ferroelectric domain walls and interfaces at the atomic level. Enabled by the pioneering work by Jia and co-workers [46–48], Chisholm *et al.* [49], Nelson and co-workers [50,51], Das *et al.* [52], and others [53–55] over a decade ago, the direct studies of domain-wall structures have become common. It has been shown that the comparison of the experimentally observed domain-wall profiles with the functional forms derived from analytical theory allows determination of the Landau-Ginzburg functional parameters, such as gradient terms and boundary conditions at the interfaces [56,57]. Very recently, this approach was extended towards the Bayesian context and the conditions for reliable elucidation of the unknown physics of materials system [58,59]. However, the availability of high-quality experimental data necessitates further development of high-veracity universal analytical models for domain-wall structure.

To fill the gap in the knowledge, here we consider the dynamics of a 180° uncharged rotational domain wall in a miltiaxial ferroelectric film within the framework of the analytical LGD approach (see Sec. II). FEM is used to solve numerically the system of the coupled nonlinear Euler-Lagrange (EL) differential equations of the second order for two components of polarization (see Sec. III). Next, using the LGD approach, we derived and analyzed the analytical solutions of the static EL equations for a polydomain 180° domain structure in a multiaxial ferroelectric film, which contain enough free parameters to satisfy arbitrary boundary conditions at the film surfaces (see Sec. IV). We analyze the domain state free-energy dependence on the film thickness and boundary conditions. Section V illustrates how the analytical solutions can be used for a Bayesian analysis of HR STEM data in thin ferroelectric films. Section VI is a brief summary. Calculation details of analytical solutions and free energy with renormalized coefficients obtained by the direct variation method are listed in Appendixes A and B, respectively, in the Supplemental Material [62].

II. PROBLEM FORMULATION

Here we consider a stress-free ferroelectric film (or layer) under the absence of free charges in it, and assume that the polarization vector **P** of the ferroelectric has a specific structure leading to the absence of a depolarization field, namely div**P** = 0. The assumption corresponds to the case of uncharged domain walls, and is consistent with the ideal screening at the interfaces. However, in the general case the depolarization fields will be present. External field is absent, since we are interested in a domain structure relaxation to a static equilibrium picture.

Without electrostriction and flexoelectric coupling, the explicit expressions of LGD energy density for polarization **P** has the form

$$G = \int (g_L + g_{\text{grad}})dv + \int g_S ds. \tag{1a}$$

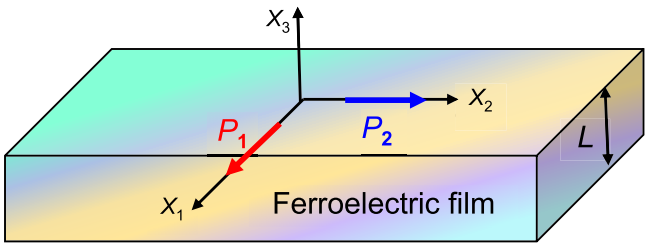

FIG. 1. The geometry of a considered multiaxial ferroelectric film with polarization vector $\boldsymbol{P}(x_3) = \{P_1(x_3),\ P_2(x_3),\ 0\}$. The film is regarded thick enough, namely its thickness $L \gg R_c$, where R_c is a correlation length.

Expressions for Landau (g_L), gradient (g_{grad}), and surface (g_S) energies in the ferroelectrics with the second-order paraelectric-ferroelectric phase transition are

$$\begin{aligned} g_L &= a_i P_i^2 + a_{ij} P_i^2 P_j^2 - P_i E_i, \\ g_{\text{grad}} &= \frac{g_{ijkl}}{2} \frac{\partial P_i}{\partial x_j} \frac{\partial P_k}{\partial x_l}, \\ g_S &= \frac{a_i^S}{2} P_i^2, \end{aligned} \tag{1b}$$

where summation is performed over all repeated indexes. As a rule, the coefficients a_i linearly depend on the temperature T, $a_i = a_{Ti}(T - T_C)$; other coefficients are temperature independent, but can be affected by elastic strains via electrostriction effect [5,6]. The surface energy coefficients a_i^S are prior unknown because they depend on the surface/interface chemistry.

Dynamic equations of state follow from the variation of action S,

$$S = \int_0^\infty dt \int \left[g_L + g_{\text{grad}} - \frac{\rho_i}{2} \left(\frac{\partial P_i}{\partial t} \right)^2 \right] dv. \tag{2}$$

The coefficient $\rho_i > 0$ in the kinetic term, $\frac{\rho_i}{2}(\frac{\partial P_i}{\partial t})^2$.

Below we consider the two-component and one-dimensional case, when the polarization vector $\boldsymbol{P}(x_3)$ depends only on the coordinate x_3 that is normal to the film surface (see Fig. 1). The vector structure $\boldsymbol{P}(x_3) = \{P_1(x_3),\ P_2(x_3),\ 0\}$ is consistent with the absence of depolarization field, since div**P** ≡ 0 in the case.

The coupled time-dependent EL equations obtained from the variation of the action (2), allowing for the Landau-Khalatnikov relaxation [60], acquire a relatively simple form:

$$\begin{aligned} &2a_1 P_1 + 4a_{11} P_1^3 + 2a_{12} P_1 P_2^2 - g_{44} \frac{\partial^2 P_1}{\partial x_3^2} \\ &= -\rho_1 \frac{\partial^2 P_1}{\partial t^2} - \Gamma \frac{\partial P_1}{\partial t}, \end{aligned} \tag{3a}$$

$$\begin{aligned} &2a_1 P_2 + 4a_{11} P_2^3 + 2a_{12} P_2 P_1^2 - g_{44} \frac{\partial^2 P_2}{\partial x_3^2} \\ &= -\rho_1 \frac{\partial^2 P_2}{\partial t^2} - \Gamma \frac{\partial P_2}{\partial t}, \end{aligned} \tag{3b}$$

where $\rho_1 > 0$ is the kinetic coefficient, and $\Gamma > 0$ is the Khalantikov coefficient. Below we assumed $m3m$

cubic symmetry of the high-temperature phase, i.e., $g_L = \sum_{i,j\neq i}(a_1 P_i^2 + a_{11} P_i^4 + a_{12} P_i^2 P_j^2 - P_i E_i)$. We note that $a_{11} > 0$, $a_{12} > -2a_{11}$, $g_{44} > 0$, $g_{11} > 0$, and $a_1^S \geqslant 0$ for the system stability; and consider negative coefficients $a_1 < 0$ corresponding to the bulk ferroelectric state at $T < T_C$.

The nonlinear coupled equations (3) are supplemented by boundary conditions at the film surfaces $x_3 = \mp\frac{L}{2}$:

$$\left(P_i - \lambda_1 \frac{\partial P_i}{\partial x_3}\right)\Big|_{x_3=-L/2} = 0,$$
$$\left(P_i + \lambda_2 \frac{\partial P_i}{\partial x_3}\right)\Big|_{x_3=+L/2} = 0, \quad i = 1,\ 2. \tag{4a}$$

Here the so-called extrapolation lengths [46,61], $\lambda_i = a_i^S/g_{44}$, are introduced. The geometric sense of λ_i is shown in Fig. S1a in the Supplemental Material [62] (see also figures in Ref. [61]). The influence of the boundary conditions (4a) on the polarization distribution is significant only in the near-surface layers of thickness several correlation lengths, $R_c = \sqrt{-g_{44}/(2a_1)}$, and is almost independent on the λ_i value. Also, the influence of λ_i value on the polarization energy decreases with the film thickness proportionally to the ratio R_c/L, since it is a typical surface effect [35,36]. In result, for thick films the number of domain walls and domains mainly contribute to the free energy, and the surface energy contribution vanishes as $1/L$.

Further let us consider the case $\lambda_1 = \lambda_2 = \lambda \geqslant 0$ corresponding to the equivalent film surfaces and positive surface energy (e.g., we regard that $a_1^S = a_2^S \geqslant 0$ for the system stability). It can be seen from Figs. S1b–S1d of the Supplemental Material [62] that the same value of λ corresponds to the solutions, which contain different numbers of domains and can be of different parity, e.g., "even" with $P_i(-\frac{L}{2}) = P_i(+\frac{L}{2})$ and $\frac{\partial}{\partial x_3} P_i(-\frac{L}{2}) = -\frac{\partial}{\partial x_3} P_i(+\frac{L}{2})$, or "odd" with $P_i(-\frac{L}{2}) = -P_i(+\frac{L}{2})$ and $\frac{\partial}{\partial x_3} P_i(-\frac{L}{2}) = \frac{\partial}{\partial x_3} P_i(+\frac{L}{2})$. Allowing for the well-known circumstance that different (meta)stable states with different numbers of domains have different energy, the number of domains can be controlled by initial conditions.

For very thick films with $L \gg 10^2 R_c$ the conditions (4a) have very little influence on the number of domains, which are determined by initial conditions, and therefore one often needs to impose some additional conditions on the polarization components, consistent with the initial conditions. Such conditions are the conditions of periodicity or antiperiodicity for every polarization component and its derivative:

$$P_i\left(-\frac{L}{2}\right) = \pm P_i\left(+\frac{L}{2}\right),$$
$$\frac{\partial}{\partial x_3} P_i\left(-\frac{L}{2}\right) = \mp \frac{\partial}{\partial x_3} P_i\left(+\frac{L}{2}\right), \quad i = 1,\ 2. \tag{4b}$$

Here the sign "+" corresponds to the periodic, and the sign "−" to the antiperiodic boundary condition. The sign choice is individual for each component.

Note that the boundary conditions (4a) and (4b) are far from equivalent, and so a smooth transition between them is absent in a general case. As a matter of fact, Eqs. (4a) are obtained from the variation of the surface and bulk free energy, and contain its parameters a_i^S (since $\lambda_i = a_i^S/g_{44}$). To the best of our knowledge Eqs. (4b), which do not contain any information about the surface energy coefficients, cannot be derived from the variational principle. Equations (4b) are additional conditions, which are imposed on the solution to minimize the surface role. Actually, the (anti)periodic conditions allow us to simulate an infinite crystal using a small computation region $\{-\frac{L}{2}, +\frac{L}{2}\}$. This approach is widespread in quantum-mechanics problems using periodic (or "cyclic") Born-Karmann boundary conditions for the solution of Schrödinger equation and in DFT calculations. In Appendix A of the Supplemental Material [62] we show that the conditions (4a) with arbitrary extrapolation lengths are more general that the conditions (4b). The full compatibility between boundary conditions (4a) and (anti)periodic conditions (4b) exists for the case $\lambda_1 = \lambda_2 = \lambda \geqslant 0$ considered in the paper. Other types of solutions, e.g., the solutions with mixed parity and without definite parity, can be realized for the cases $\lambda_1 = -\lambda_2 = \lambda > 0$ and $\lambda_1 \neq -\lambda_2$, respectively. For these cases the boundary conditions (4a) are incompatible with the conditions (4b).

The first integral of the system (3) is $I(\boldsymbol{x}) = g_L - g_{\text{grad}}$. The conservation of this dynamic invariant, $I(\boldsymbol{x}) = \text{const}$, means that the system tendency to lower the domain-wall energy (coming from the gradient energy g_{grad}) is compensated by the ferroelectric nonlinearity energy (coming from the Landau energy g_L). For FEM simulations, initial distributions are taken either in the form of a random small-amplitude polarization, or in the form of a solitary domain wall with superimposed random fields, or in the form of a small-amplitude sinusoidal modulation.

III. EQUILIBRIUM STRUCTURE OF TWO-COMPONENT DOMAIN WALLS

A. Finite element modeling of a solitary domain wall

Here we analyze the structure of the equilibrium uncharged 180° domain walls in the second-order ferroelectric, which are relaxed solution of Eqs. (3). To analyze the domain-wall structure, we introduce the dimensionless coordinate x, film thickness l, polarization components p_1 and p_2, ferroelectric anisotropy factor μ, relaxation time τ, and kinetic coefficient ρ:

$$x = \frac{x_3}{R_c}, \quad l = \frac{L}{R_c}, \quad p_1 = \frac{P_1}{P_S}, \quad p_2 = \frac{P_2}{P_S},$$
$$\mu = \frac{a_{12}}{2a_{11}}, \quad \tau = -\frac{\Gamma}{a_1}, \quad \rho = -\frac{\rho_1}{a_1}. \tag{5}$$

Here $P_S = \sqrt{-a_1/(2a_{11})}$ is the spontaneous polarization value, and $R_c = \sqrt{-g_{44}/(2a_1)}$ is a correlation length (see Appendix A in the Supplemental Material for details [62]). For multiaxial perovskite-type ferroelectrics with

ferroelectric Curie temperature >400 K (e.g., $BaTiO_3$, $(Pb, Zr)TiO_3$, $BiFeO_3$, etc.), the values $P_S = (0.25 - 1)$ C/m^2 and $R_c = (0.2 - 2)$ nm at room temperature (see Table SI in Appendix A [62]). Thus, the dimensionless thickness $l = 100$ corresponds to sufficiently thin films with $l = (20 - 200)$ nm. The anisotropy factor μ varies from -0.2 to $+4.5$ and, as a rule, is temperature-independent (except for, e.g., $BaTiO_3$; see Table SII [62]).

In fact, we postulated that the continuum media LGD approach is valid, and, using it, solved Euler-Lagrange equations. The only *criteria* for the quantitative validity of the LGD approach is the scale of continuous calculations—a correlation radius R_c, which is equal to $\sqrt{-g_{44}/(2a_1)}$ for the ferroelectric with the second-order phase transition. R_c is temperature dependent since $a_1 = \alpha_T(T - T_C)$. The apparent domain-wall width is calculated numerically or analytically in R_c units. The scale R_c can be written in the form $R_c = R_0\sqrt{T_C/(T_C - T)}$, where $R_0 = \sqrt{g_{44}/(2\alpha_T T_C)}$ and $T < T_C$. R_c must be more that several lattice constants for semiquantitative validity of LGD approach [36]. When $2R_c$ well exceeds ten lattice constants LGD results become quantitatively valid. Since R_c is minimal at $T = 0$ K and diverges at $T \to T_C$, its minimal value R_0 defines the ranges of LGD approach validity far from T_C. The value $\alpha_T T_C$ are well known and tabulated for most inorganic perovskite ferroelectrics. However, since the gradient coefficients g_{ijkl} demonstrate a wide discrepancy (from 1 to 2 orders of magnitude) from indirect experiments, such as HR STEM and piezoresponse force microscopy (PFM) measurements of the apparent domain-wall width in pristine and doped ferroelectrics, grown in the form of single crystals or sintered in the form of thin films, and the values of g_{ijkl} calculated from DFT can strongly vary in sign and magnitude, the discrepancy of R_0 is rather strong (see Table SI and references therein [62]). The reason for this discrepancy can be dopants (cations or vacancies), elastic strains in thin films, and oxygen octahedra tilt in antiferrodistortive perovskites.

It is seen from Table SI [62] that $2R_0$ is not less than a lattice constant (0.4 nm) for all cases, but can be very close to the value for $g_{44} \cong 10^{-10}\,C^{-2}m^3\,J$ and $a_1 \cong 10^7\,C^{-2}\,J\,m/K$ questioning the applicability of LGD approach for the cases. However, a surprising conclusion has been made in several papers, which compares the domain-wall profiles, measured experimentally or/and calculated from DFT and LGD. It appeared that LGD is still applicable quantitatively for Ising, Ising-Néel, Ising-Bloch-type walls in $PbTiO_3$, when $2R_c$ is about one lattice constant (see, e.g., Figs. 11 and 12 in Ref. [40]). LGD is certainly valid for the case of the purely Bloch-type walls in $BaTiO_3$, as their width reaches the value of about several nanometers even far from the paraelectric-ferroelectric phase-transition point (see, e.g., Refs. [37,38] and Fig. 6 for 250 K $< T <$ 350 K in Ref. [42]), and $BiFeO_3$ (compare Figs. 2 and 4 with Figs. 6–8 in Ref. [9]). Besides these examples for classical perovskites $PbTiO_3$, $BaTiO_3$, and $BiFeO_3$, the modern material science and advanced nanotechnology allow us to tailor a great versatility of synthetized ferroelectric materials (both classical and exotic), whose gradient energy parameters (determining g_{44}) and the ratio "anisotropy/exchange" (determining μ) can vary in a very wide range. Since we are mainly interested in the Bloch-Ising domain-wall structure and obtained analytical solutions for the case, the above examples and facts give us solid grounds for applying LGD theory in a wide temperature range without any concrete reference to concrete material.

The dimensionless EL equations, obtained from dynamic Eqs. (3), have the form

$$-\rho\frac{\partial^2 p_1}{\partial t^2} - \tau\frac{\partial p_1}{\partial t} = -\frac{\partial^2}{\partial x^2}p_1 - p_1 + p_1^3 + \mu p_1 p_2^2, \quad (6a)$$

$$-\rho\frac{\partial^2 p_2}{\partial t^2} - \tau\frac{\partial p_2}{\partial t} = -\frac{\partial^2}{\partial x^2}p_2 - p_2 + p_2^3 + \mu p_2 p_1^2. \quad (6b)$$

To study the polarization relaxation to a stable or metastable state, we set $\rho = 0$ and chose the calculation time $t_{\max}$ much higher than the time τ of the polarization relation to an equilibrium state, e.g., $t_{\max} \gg 100\ \tau$. Initial distribution of polarization used in FEM is chosen in the form of a solitary Ising-type domain wall perturbed by a small fluctuation:

$$p_1(x,\ t = 0) = p_0 \tanh\left(\frac{x}{b}\right) + \delta p_1(x),$$
$$p_2(x, t = 0) = \delta p_2(x), \quad (7a)$$

where the random fluctuation $|\delta p_{1,2}(x)| \ll |p_0|$.

The boundary conditions (4a) in the dimensionless variables acquire the form

$$\left(\frac{p_1}{\lambda_1} \mp \frac{\partial p_1}{\partial x}\right)\Big|_{x=\mp l/2} = 0,\ \left(\frac{p_2}{\lambda_2} \mp \frac{\partial p_2}{\partial x}\right)\Big|_{x=\mp l/2} = 0. \quad (7b)$$

Here $\frac{1}{\lambda_i} = \frac{a_i^S}{g_{44}R_c}$ $(i = 1,\ 2)$ are the dimensionless inverse extrapolation lengths, which are not negative, and can vary in a very wide range, $0 \leqslant \lambda_i < \infty$, due to uncertainty of available experimental parameters. For the case $\frac{1}{\lambda_i} > 0$ and $l < 100$, either a solitary domain wall or a periodic domain structure appears after the polarization relaxation to an equilibrium state. In this work we mostly consider the case $\frac{1}{\lambda_i} = 0$ (i.e., very high $\lambda_i \to \infty$), which corresponds to the "natural" boundary conditions, $\frac{dp_i}{dx}|_{x=\pm l/2} = 0$ [i.e., zero surface energy in Eq. (1a)], and the alternative, $\lambda_i = 0$, which corresponds to $p_i|_{x=\pm l/2} = 0$.

The antiperiodic-periodic conditions (4b) consistent with the initial condition (7a) and boundary conditions (7b), which will be used for thick films with $l \gg 100$, have the form

$$p_1\left(-\frac{l}{2}\right) = -p_1\left(\frac{l}{2}\right), \quad \frac{\partial p_1}{\partial x}\Big|_{-\frac{l}{2}} = \frac{\partial p_1}{\partial x}\Big|_{\frac{l}{2}},$$
$$p_2\left(-\frac{l}{2}\right) = p_2\left(\frac{l}{2}\right), \quad \frac{\partial p_2}{\partial x}\Big|_{-\frac{l}{2}} = -\frac{\partial p_2}{\partial x}\Big|_{\frac{l}{2}}. \quad (7c)$$

The boundary problem (6) and (7) depends on the only control parameter—ferroelectric anisotropy factor μ. The inequality $-1 < \mu$ should be valid for the system stability. The numerical solutions of Eqs. (6) are shown in Figs. 2(a)–2(f) for several values of the anisotropy factor μ.

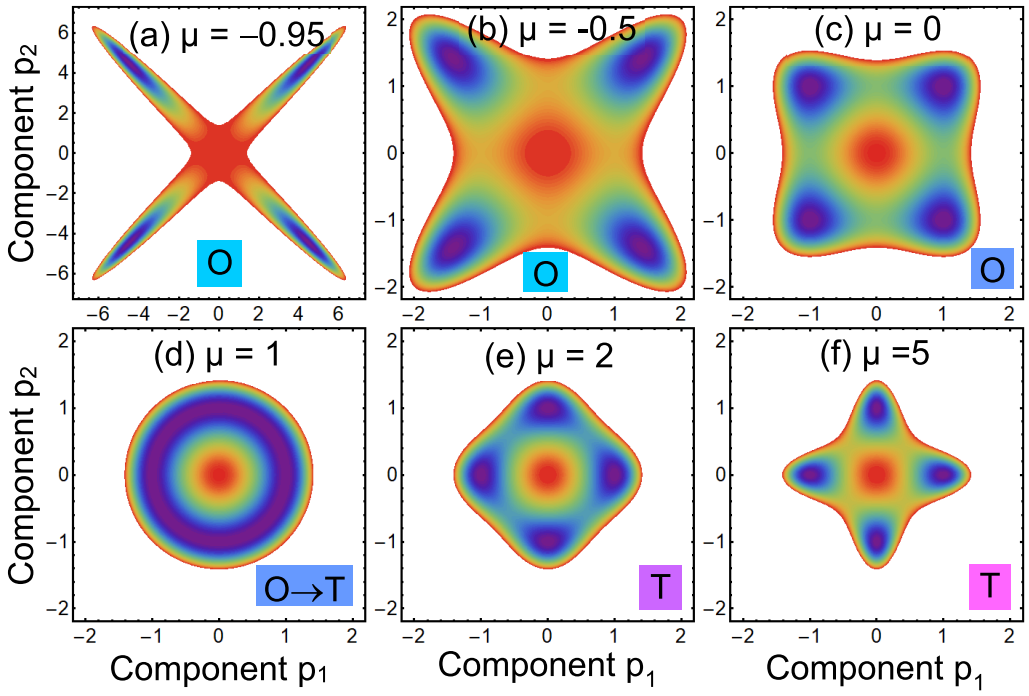

FIG. 2. The free energy (8) as a function of order parameter components p_1 and p_2 for different values of parameter μ: (a) $\mu = -0.95$, (b) $\mu = -0.5$, (c) $\mu = 0$, (d) $\mu = 1$, (e) $\mu = 2$, and (f) $\mu = 5$. Red color denotes zero energy, while violet color is its minimal density equal to -10 (a), -1 (b), $-1/2$ (c), and $-1/4$ (d)–(f) relative units. Capital letters "O" and "T" denote orthorhombic and tetragonal spatially homogeneous phases, respectively.

The dimensionless LGD free energy density and the first integral corresponding to Eqs. (6) have the form

$$G = \int_{-l/2}^{l/2} g_V(x)dx + \frac{p_1^2(-l/2)}{\lambda_1} + \frac{p_2^2(-l/2)}{\lambda_2} + \frac{p_1^2(l/2)}{\lambda_1} + \frac{p_2^2(l/2)}{\lambda_2}, \tag{8a}$$

$$g_V = -\frac{1}{2}(p_1^2 + p_2^2) + \frac{1}{4}(p_1^4 + p_2^4) + \frac{\mu}{2}p_1^2p_2^2 + \frac{1}{2}\left[\left(\frac{dp_1}{dx}\right)^2 + \left(\frac{dp_2}{dx}\right)^2\right], \tag{8b}$$

$$I_1[\mu] = -\frac{1}{2}(p_1^2 + p_2^2) + \frac{1}{4}(p_1^4 + p_2^4) + \frac{\mu}{2}p_1^2p_2^2 - \frac{1}{2}\left[\left(\frac{dp_1}{dx}\right)^2 + \left(\frac{dp_2}{dx}\right)^2\right] = \begin{cases} \frac{-1}{2(1+\mu)}, & -1 < \mu < 1, \\ -\frac{1}{4}, & \mu > 1. \end{cases} \tag{8c}$$

The free energy (8) as a function of polarization components p_1 and p_2 is shown in Fig. 2 for different μ values and zero gradients consistent with the case $\lambda_i \to \infty$. Two spatially homogeneous phases (8) exist, namely as follows:

(1) Orthorhombic O phase with the minimal energy density $g_{\rm LGD} = -\frac{1}{2(1+\mu)}$ corresponding to polarization components $p_1 = p_2 = \pm\frac{1}{\sqrt{1+\mu}}$ [see Figs. 2(a)–2(c)]. The O phase is stable at $-1 < \mu < 1$.

(2) Tetragonal T phase with the minimal and energy density $g_{\rm LGD} = -\frac{1}{4}$ corresponding to polarization components $p_1^2 = 1$, $p_2^2 = 0$, or $p_1^2 = 0$, $p_2^2 = 1$ [see Figs. 2(e) and 2(f)]. The T phase is stable at $\mu > 1$. The $O \to T$ transition takes place at $\mu = 1$, when the four potential minima merge and transform in a circle [see Figs. 2(d)].

A detailed analysis of FEM results allows concluding that we can distinguish (somewhat arbitrarily) several different morphologies of the domain wall, shown in Figs. 3(a)–3(f), where the control parameter μ determines the structure of the uncharged 180° domain walls and values of polarization components p_i. The description of these areas is the following:

(1) The first region, "1," where $-1 < \mu < 0$, corresponds to the O phase with Ising-Bloch domain walls [see Fig. 3(a)]. Far from the wall (i.e., at $x \to \pm\infty$) the saturation expressions, $p_1 \to \pm\frac{1}{\sqrt{1+\mu}}$ and $p_2 \to +\frac{1}{\sqrt{1+\mu}}$, are valid for the polarization components. Thus $|p_1| = |p_2| > 1$ far from the wall. The component p_1 has an antisymmetric tanhlike profile across the domain wall; and the component p_2 has a symmetric profile with a sharp minimum well-localized at the wall. The minimum height decreases with μ increase, and disappears at $\mu \to 0$ [see Fig. 3(b)]. Because p_1 is zero and p_2 is minimal at the wall, the contrast of the HR STEM image across the wall looks like a "dark-dark" pattern for $-1 < \mu < 0$.

(2) The second region, "2," where $0 < \mu < 1$, corresponds to the O phase with Ising-Bloch domain walls [see Fig. 3(c)]. The expressions $p_1 \to \pm\frac{1}{\sqrt{1+\mu}}$ and $p_2 \to \pm\frac{1}{\sqrt{1+\mu}}$ are valid far from the wall, where $|p_1| = |p_1| < 1$. The

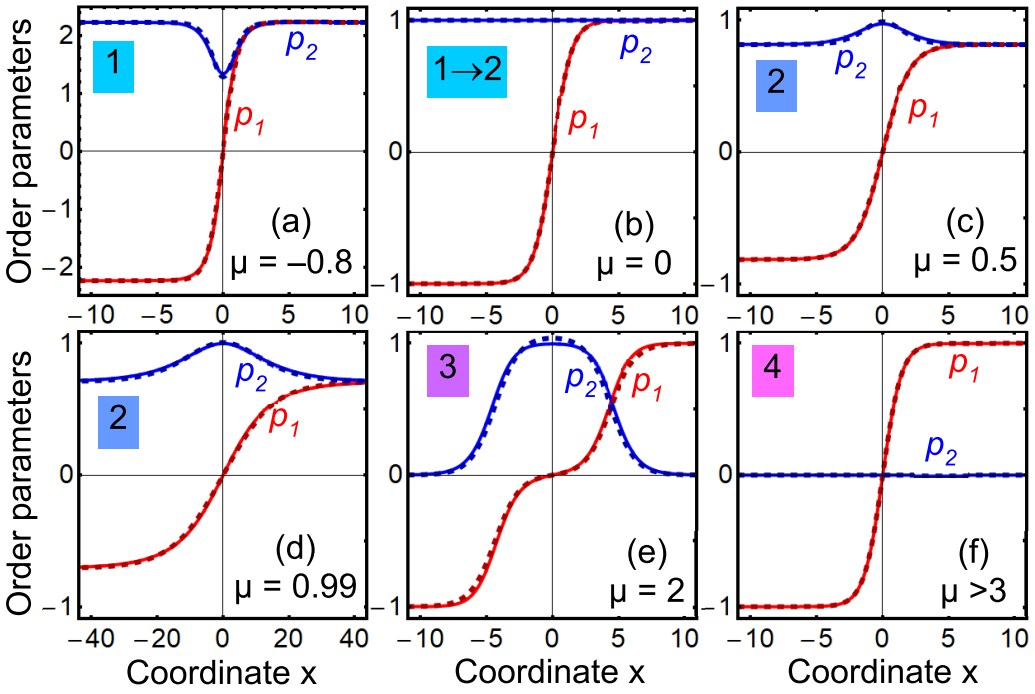

FIG. 3. Profiles of polarization components p_1 (red curves) and p_2 (blue curves) calculated for different values of ferroelectric anisotropy μ: (a) $\mu = -0.8$, (b) $\mu = 0$, (c) $\mu = 0.5$, (d) $\mu = 0.99$, (e) $\mu = 2$, and (f) $\mu = 4$. Solid and dashed curves represent FEM solution of Eqs. (6) and its fitting with the trial functions (9), respectively. Numbers 1–4 denote the regions with different morphology of domain wall: "1" is for the Ising-Bloch domain wall in the O phase; "1 → 2" is for the Ising wall at the domain boundary; "2" is for the simple Ising-Bloch domain wall in the O phase, "3" for is for the steplike Ising-Bloch-type domain wall in T phase; and "4" is for the purely Ising domain wall in T phase. Film thickness $l \gg 100$.

component p_1 has an antisymmetric tanhlike profile across the domain wall; and the component p_2 has a symmetric profile with a maximum at the wall. Both the domain-wall width for the p_1 and p_2 components and the maximum height for the p_1 component increase with μ increase; at that the wall becomes very thick and diffuse at $\mu \to 1$ [see Fig. 3(d)]. At $\mu = 1$ the value $p_1^2 + p_2^2$ is invariant, and so the exceptional case of "isotropic" ferroelectric is realized by solution of Eqs. (6). Because p_1 is zero and p_2 has a sharp maximum at the wall, the contrast of the HR STEM image across the wall looks like a "dark-bright" thin pattern for $0 < \mu < 1$.

(3) The third region, "3," where $1 < \mu < 3$, corresponds to the T phase with mixed-type Ising-Bloch domain walls [see Fig. 3(e)]. Far from the wall, where $p_1 \to \pm 1$ and $p_2 \to 0$. The component p_1 has an antisymmetric double-step-like profile across the domain wall, and the component p_2 has a symmetric profile with a flat maximum that is centered at the wall. Both the step width for p_1 and the height and width of p_2 maximum gradually decrease with μ increase, and eventually disappears at $\mu = 3$. An energy estimate shows that steplike Ising-Bloch and purely Ising walls coexist at $\mu = 3$. Because p_1 has a zero plateau and p_2 has a flat maximum at the wall, the contrast of the HR STEM image across the wall looks like a "dark-bright" thick pattern for $1 < \mu < 3$.

(4) The fourth region, "4," where $\mu > 3$, corresponds to the T phase with purely Ising-type domain walls [see Fig. 3(f)]. The component p_2 is absent and the component p_1 has an antisymmetric tanhlike profile across the domain wall and saturates far from the wall, where $p_1 \to \pm 1$. Since $p_2 \equiv 0$, the domain-wall profile is μ independent. Because p_1 is zero at the wall and p_2 is absent, the contrast of the HR STEM image across the wall looks like a "dark" pattern for $\mu > 3$.

B. Analytical solutions for a solitary domain wall in a thick film

To find equilibrium analytical solutions, the direct variational method is applied for Eqs. (6) using the trial functions in the form of two kinks superposition and constants:

$$p_1(x) = a_0 + \frac{a_1}{2}\left[\tanh\left(\frac{x + x_w}{w}\right) + \tanh\left(\frac{x - x_w}{w}\right)\right], \quad (9a)$$

$$p_2(x) = a_2 + \frac{b_2}{2}\frac{w}{x_w}\left[\tanh\left(\frac{x + x_w}{w}\right) - \tanh\left(\frac{x - x_w}{w}\right)\right]. \quad (9b)$$

The constant amplitude $a_0 \equiv 0$ to satisfy the antisymmetric boundary conditions for $p_1(x)$ [see Eqs. (7c)]. The amplitudes a_1 and a_2 define polarization components far from the wall, because $p_1(x \to \pm\infty) \to \pm a_1$ and $p_2(x \to \pm\infty) \to a_2$. The amplitude b_2 contributes to the p_2 extremum at the wall, since $p_2(0) \to a_2 + b_2 \frac{w}{x_w} \tanh(\frac{x_w}{w})$. The length w and shift x_w define the width of the $p_1(x)$ and $p_2(x)$ domain walls. These five variational parameters can be determined after substitution of Eqs. (9) in the free energy (7), further integration and minimization of the free energy over these parameters. This allows us to obtain analytical dependencies for the variational parameters on the control parameter μ (see Appendix B in the Supplemental Material [62]).

TABLE I. Parameters in Eqs. (9) corresponding to exact solution of the Eqs. (6), and limiting cases[a].

	Parameters in Eqs. (9)				
μ value	Amplitude a_1	Amplitude a_2	Amplitude b_2	Width w	Shift x_w
$\mu \to -1$	tends to $+\infty$	tends to $+\infty$	tends to $-\infty$	$\sqrt{2}$	0, as defined from B.C.[b]
$\mu = 0$	1	1	0	$\sqrt{2}$	0, as defined from B.C.[c]
$\mu \to 1$	undefined	undefined	undefined	diverges	undefined[d]
$\mu = 3$	1	0	1	$\sqrt{2}$	undefined[e]
$\mu > 3$	1	0	0	$\sqrt{2}$	0, as defined from B.C.

[a]The constant amplitude $a_0 \equiv 0$ to satisfy the antisymmetric boundary conditions for $p_1(x)$.
[b]The abbreviation "B.C." means boundary conditions.
[c]For $\mu = 0$ the equations become decoupled.
[d]For $\mu = 1$ the first-order phase transition occurs in domain morphology.
[e]For $\mu = 3$ the energy is x_w independent.

The choice of the trial functions (9) is based on the fact that the functions are exact and stable solutions of Eqs. (6) for zero anisotropy, $\mu = 0$, and relatively high anisotropy, $\mu \geqslant 3$. Corresponding values of parameters a_1, a_2, b_2, w, and x_w are listed in Table I**.** The solution (9) also describes the instability limit at $\mu \to -1$ and the first-order phase transition at $\mu = 1$ (see Table I for details). When we impose the antiperiodic-periodic conditions (7c) for FEM results, the shift x_w should be zero for the stability of the numerical solution in thick films at $-1 < \mu < 1$ (O phase) and $\mu > 3$ (T phase).

The variational procedure makes sense only if the trial functions (9) correspond to sufficiently accurate fitting of the numerically calculated domain-wall profiles. To verify this, we performed FEM at $l \gg 100$ imposing antiperiodic-periodic conditions (7c), and obtained that the functions (9) surprisingly well fit the numerical profiles point-in-point for all μ values in the range $-1 < \mu < 5$ (compare solid and dashed curves in Figs. 3).

From the fitting of FEM results we extracted the variational parameters a_1, a_2, b_2, w, and x_w, whose dependencies on μ are presented in Figs. 4(a) and 4(b). Using the direct variational method, we derived simple analytical expressions for the μ dependence of the amplitudes a_1 and a_2:

$$a_1 = \begin{cases} \pm\sqrt{\frac{1}{1+\mu}}, & -1 < \mu < 1, \\ \pm 1, & \mu > 1, \end{cases}$$
$$a_2 = \begin{cases} \pm\sqrt{\frac{1}{1+\mu}}, & -1 < \mu < 1, \\ 0, & \mu > 1. \end{cases} \qquad (10a)$$

Expressions (10a) are almost exact [see blue and black curves in Fig. 4(a), where the case corresponding to the sign "+" is shown]. Using the conservation of the first integral at the domain wall and Eqs. (10a), we derived approximate expressions for the amplitude b_2:

$$b_2 \approx \begin{cases} \mp\sqrt{\frac{1}{1+\mu}} \mp 1, & -1 < \mu < 1, \\ \pm\frac{x_w}{w}\coth\left(\frac{x_w}{w}\right), & 1 < \mu < 3, \\ 0, & \mu > 3. \end{cases} \qquad (10b)$$

The upper signs in the expression (10b) corresponds to red curves in Fig. 4(a).

The domain-wall width w and shift x_w have a strong peculiarity in the same region $0.9 < \mu < 1.1$ and can be approximately described by the spline-interpolation functions:

$$w \approx \begin{cases} \text{spline}, & -1 < \mu < 1, \\ \text{spline}, & 1 < \mu < 3, \\ \sqrt{2}, & \mu > 3, \end{cases}$$
$$x_w \approx \begin{cases} 0, & -1 < \mu < 1, \\ \text{spline}, & 1 < \mu < 3, \\ 0, & \mu > 3. \end{cases} \qquad (10c)$$

Expressions (10c) correspond to brown and green curves in Fig. 4(b). The variational method determining the analytical

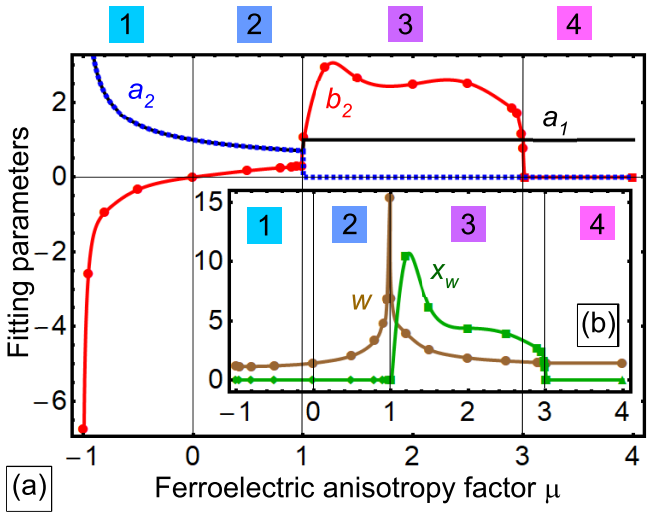

FIG. 4. (a) Dependencies of the polarization amplitudes a_1, a_2, and b_2 (solid black, blue dotted, and solid red curves respectively) on the control parameter—ferroelectric anisotropy factor μ. (b) Dependencies of the shift x_w and width w on the parameter μ (green and brown curves respectively). Numbers 1–4 in the upper row denote regions with different morphology of domain walls, whose profiles are shown in Fig. 2. Regions "1" and "2" correspond to the "dark-dark" and "dark-bright" Ising-Bloch domain walls in O phase; regions "3" and "4" correspond to the mixed Ising-Bloch and purely Ising domain walls in T phase. Solid, green, and brown curves are spline-interpolations plotted through the symbols (circles and boxes) calculated by FEM.

dependencies of parameters a_1, a_2, b_2, w, and x_w on μ is described in Appendix B in the Supplemental Material [62].

The high accuracy of the fitting results (shown in Figs. 3 and 4) in the entire range $-1 < \mu < 5$, which uses only five $\mu-$ dependent parameters for two polarization components, allows us to conclude that the analytical functions (9), which are trial functions in the direct variational method, can be treated as the high-accuracy variational solution of the static EL equations with cubic nonlinearity.

IV. ANALYTICAL POLYDOMAIN SOLUTIONS

A. Analytical polydomain solutions for the "rotational" walls

For the case of negative ferroelectric anisotropy factor $\mu \leqslant -1$ the system of Eqs. (6a) becomes unstable. Here we explore stable polydomain solutions of Eqs. (6) for the case $\mu > -1$ and $l < 100$. After introducing new variables in Eqs. (6), $p = p_1 + p_2$ and $a = p_1 - p_2$, one could get the following equations for them [see Eq. (A.5b) in Appendix A of the Supplemental Material [62]]:

$$-p + \frac{1+\mu}{4}p^3 + \frac{3-\mu}{8}p\,a^2 - \frac{\partial^2 p}{\partial x^2} = 0, \tag{11a}$$

$$-a + \frac{1+\mu}{4}a^3 + \frac{3-\mu}{8}a\,p^2 - \frac{\partial^2 a}{\partial x^2} = 0. \tag{11b}$$

It is seen that Eqs. (11a) and (11b) are independent of each other for the specific case $\mu = 3$, when they can be solved separately using elliptic Jacobi functions. The solution for $\mu = 3$ has the form of elliptic sine ("snoid") functions:

$$p(x_3) = \sqrt{\frac{2m}{1+m}}\,sn\left(\frac{x+x_{w1}}{\sqrt{1+m}}\middle|m\right),$$
$$a(x_3) = \sqrt{\frac{2n}{1+n}}\,sn\left(\frac{x+x_{w2}}{\sqrt{1+n}}\middle|n\right), \tag{12}$$

where two "modules," $0 \leqslant m \leqslant 1$ and $0 \leqslant m \leqslant 1$, and two "shifts," x_{w1} and x_{w2}, of snoids should be defined from the boundary conditions, as shown below.

Next, using the relations $p_1 = (p+a)/2$ and $p_2 = (p-a)/2$, one obtains from Eqs. (12) the expressions for p_1 and p_2 in the form of two snoids superposition:

$$p_1(x) = \frac{1}{2}\left[\sqrt{\frac{2m}{1+m}}\,\mathrm{sn}\left(\frac{x+x_{w1}}{\sqrt{1+m}}\middle|m\right) + \sqrt{\frac{2n}{1+n}}\,\mathrm{sn}\left(\frac{x+x_{w2}}{\sqrt{1+n}}\middle|n\right)\right], \tag{13a}$$

$$p_2(x) = \frac{1}{2}\left[\sqrt{\frac{2m}{1+m}}\,\mathrm{sn}\left(\frac{x+x_{w1}}{\sqrt{1+m}}\middle|m\right) - \sqrt{\frac{2n}{1+n}}\,\mathrm{sn}\left(\frac{x+x_{w2}}{\sqrt{1+n}}\middle|n\right)\right]. \tag{13b}$$

Since the solution (13) is dependent on four free parameters, modules m and n and shifts x_{w1} and x_{w2}, it pretends to be a general solution, but we cannot say that it is the one, because the existence and uniqueness theorem is not valid for solutions of nonlinear differential equations. The modules m and n define the shape and the period of the polarization profile (13).

1. Natural and zero boundary conditions for the polarization components

It is shown in Appendix A in the Supplemental Material [62] that the modules m and n satisfy the same transcendental equations for the two limiting cases of the boundary conditions (7b), $\lambda_i = 0$ and $\lambda_i \to +\infty$, namely

$$2\sqrt{1+m}\mathbf{K}(m)N_x = l,$$
$$2\sqrt{1+n}\,\mathbf{K}(n)N_y = l. \tag{14a}$$

Here $\mathbf{K}(k)$ is the complete elliptic integral of the first kind, which determines the half-period $2\mathbf{K}(k)$ of the elliptic functions. Also we introduced the numbers $N_x = 0,\ 1,\ 2\ldots$ and $N_y = 0,\ 1,\ 2,\ \ldots$ corresponding to the number of "nodes" of $p(x)$ and $a(x)$ functions, which satisfy Eqs. (11a) and (11b), respectively. The situation with these nodes is similar to the eigensolutions of a wave equation, when the boundary conditions are satisfied by an infinite set of solutions with a different number of half waves for a fixed thickness l.

At the same time, we obtained that the shifts x_{w1} and x_{w2} depend on the boundary condition type, namely, and for the natural boundary conditions $\frac{dp_i}{dx}|_{x=\pm l/2} = 0$ they have a relatively simple form:

$$x_{w1} = \frac{l}{2}\left(1 \pm \frac{1}{N_x}\right),$$
$$x_{w2} = \frac{l}{2}\left(1 \pm \frac{1}{N_y}\right), \quad (\lambda_i \to +\infty). \tag{14b}$$

For zero polarization conditions $p_i|_{x=\pm l/2} = 0$ the shifts are given by more complex expressions

$$x_{w1} = \frac{l}{2}\left(1 \pm \frac{1-(-1)^q}{N_x}\right),$$
$$x_{w2} = \frac{l}{2}\left(1 \pm \frac{1-(-1)^s}{N_y}\right), \quad (\lambda_i = 0), \tag{14c}$$

where q and s are independent integers. From Eqs. (14) the par of integers $\{N_x, N_y\}$ characterizes the domain structure of the solution (13) at a given l. However, the characterization is not unique due to the two possible signs "±" and different powers q and s in Eqs. (14b) and (14c).

The case $N_x = 0$ (or $N_y = 0$, or both) requires a separate consideration, since it corresponds to the limiting cases $m \to 1$ (or/and $n \to 1$), respectively. The shift $x_{w1,2}$ diverges as $-\ln(\sqrt{1-k})$ at $k \to 1$ ($k = m, n$) and the solutions (12) and (13) formally become undefined. More rigorous consideration shows that the case corresponds to "nodeless" solutions, which are trivial and independent on the film thickness,

$$p(x_3) \overset{N_x \to 0}{\to} \begin{cases} 0, & \lambda_i = 0, \\ 1, & \lambda_i \to +\infty, \end{cases}$$
$$a(x_3) \overset{N_y \to 0}{\to} \begin{cases} 0, & \lambda_i = 0, \\ 1, & \lambda_i \to +\infty. \end{cases} \tag{14d}$$

Using the "decoupled" form (12) of the solution (13) in a general case, the "decoupled" free energy, $G[p, a]$, is equal to

$$G[p,a] = \frac{1}{l}\int_{-\frac{l}{2}}^{\frac{l}{2}} dx\left\{ -\frac{p^2+a^2}{4} + \frac{p^4+a^4}{8} + \frac{1}{4}\left[\left(\frac{dp}{dx}\right)^2 + \left(\frac{da}{dx}\right)^2\right]\right\} \equiv G[m,n], \quad (15a)$$

$$G[m,n] = G_c[m] + G_c[n],$$

$$G_c[k] = -\frac{1}{6(1+k)^2}\left(2+k-2(1+k)\frac{\mathbf{E}(k)}{\mathbf{K}(k)}\right), \quad (15b)$$

where $\mathbf{E}(k)$ is the complete elliptic integral of the second type. Since the energy is independent on $x_{w1,\,2}$, it is the same for both cases $\lambda_i = 0$ and $\lambda_i \to +\infty$. The case $m \to 1$ (or $n \to 1$) is exceptional, and corresponding contributions to Eq. (15a) should be rewritten as follows:

$$G_c[m] \overset{N_x\to 0}{\to} \begin{cases} 0, & N_x \to 0, \quad \lambda_i = 0; \\ -\frac{1}{8}, & N_x \to 0, \quad \lambda_i \to +\infty. \end{cases} \quad (15c)$$

The normalized energy $G[m, n]$ of the polydomain states as a function of l was calculated from Eqs. (15) for different numbers of domain walls inside the film, $\{N_x, N_y\}$. Results are shown in Fig. 5(a) for $\lambda_i \to +\infty$, and in Fig. 6(b) for $\lambda_i = 0$. The energy is normalized on a "bulk" value $G_b = 1/4$. Typical distribution of polarization components p_1 (red curves) and p_2 (blue curves) calculated with Eqs. (13) for different N_x and N_y are shown in Figs. 5(b)–5(g) for $\lambda_i \to +\infty$, and in Figs. 6(b)–6(g) for $\lambda_i = 0$.

The metastable and stable polydomain states have negative energy, which monotonically decreases with l increase for a fixed $\{N_x, N_y\}$ in both cases $\lambda_i \to +\infty$ and $\lambda_i = 0$ [see Figs. 5(a) and 6(a)]. The single-domain state with $N_x = N_y = 0$ is absolutely stable for $\lambda_i \to +\infty$ (corresponding energy relief corresponds to the potential well) and unstable for $\lambda_i = 0$ (corresponding energy relief corresponds to the saddle point) [compare horizontal dashed lines in Figs. 5(a) and 6(a)]. The critical thickness of the film, l_{cr}, below which the ferroelectric phase disappears, is individual for the concrete polydomain state $\{N_x, N_y\}$, and, as a rule, it increases with sum $N_x + N_y$ increase [see vertical dotted lines in Figs. 5(a) and 6(a)]. Only the single-domain state $\{0, 0\}$ has no critical thickness at $\lambda_i \to +\infty$. The states $\{0, 1\}$, $\{1, 1\}$, $\{1, 2\}$, $\{1, 3\}$ … and $\{1, N\}$ have the same minimal $l_{cr} \approx \pi$. The states $\{0, 2\}$, $\{2, 2\}$, $\{2, 3\}$, … and $\{2, N\}$ have the same $l_{cr} \approx 2\pi$. The states $\{0, 3\}$, $\{3, 3\}$, $\{3, 4\}$, … and $\{3, N\}$ have the same $l_{cr} \approx 3\pi$. In general, all states with the same $N = \min\{N_x, N_y\}$ have the same $l_{cr}[N]$, which increases with N increase. The critical thickness can be derived from Eqs. (14a) in the limit $m \to 0$ (or $n \to 0$), namely

$$l_{cr}[N] \approx \pi N \quad (N > 0). \quad (16)$$

For a fixed l and $\lambda_i \to +\infty$ the energy of the polydomain states increases with the sum $N_x + N_y$ increase [see Fig. 5(a)], and the lowest polydomain state is $\{0, 1\} = \{1, 0\}$. The energy of $\{0, 2\}$ state is slightly lower that the energy of $\{1, 1\}$ state, but this state has twice bigger l_{cr}. For $l > l_{cr}$ the energies of $\{1, 1\}$ and $\{0, 2\}$ states become very close and approach the energy of the single-domain state in the limit $l \gg l_{cr}$. The same trend is evident for all other states $\{N_x, N_y\}$ and $\{0, N_x + N_y\}$. It is important that the energy of all polydomain states tends to the single-domain state energy $G = -G_b$ in the limit $l \to +\infty$ for the case $\lambda_i \to +\infty$.

It is seen from Figs. 5(b)–5(g) that the profile and amplitude of the polydomain solution (13) is determined by the film thickness l and by the "nodes" pair $\{N_x, N_y\}$. Simple Ising-type domains with quasisinusoidal profile for l slightly bigger than l_{cr} [see Fig. 5(b)], or with strongly anharmonic "snoidal" profile for $l \gg l_{cr}$ [see Fig. 5(e)], correspond to the same numbers $N_x = N_y$. Rather complex phase-shifted asymmetric Bloch-Ising type profiles, which are quasiharmonic for $l \approx l_{cr}$ [see Fig. 5(c)] and strongly anharmonic for $l \gg l_{cr}$ [see Fig. 5(f)], correspond to the close numbers $N_x = N_y - 1$. Simple in-phase [i.e., $p_1(x) = p_2(x) + 1$] and symmetric [i.e., $p_{1,2}(x) = p_{1,2}(-x)$] Bloch-Ising-type profiles, which are quasiharmonic for $l \approx l_{cr}$ [see Fig. 5(d)], and strongly anharmonic for $l \gg l_{cr}$ [see Fig. 5(g)], correspond to the pairs $\{0, N_y\}$ or $\{N_x, 0\}$.

For a fixed l and $\lambda_i = 0$ the energy of the polydomain states increases with N_x or/and N_y increase [see Fig. 6(a)], and the lowest polydomain states are $\{1, 1\}$, $\{1, 2\}$, and $\{1, 3\}$, respectively. The energy of the $\{0, 1\}$ state is almost the same as the energy of the $\{1, 3\}$ state only for $l < 3\pi$; at $l \gg 3\pi$ it tends to $-G_b/2$, while the energy of the $\{1, N_y\}$ states tends to $-G_b$ in the limit $l \gg l_{cr}$. The same trend is evident for all other states $\{N_x, N_y\}$ ($N_{x,y} \geqslant 1$), whose energy eventually tends to $-G_b$ in the limit $l \to +\infty$. The energy of $\{0, N_y\}$ eventually tends to $-G_b/2$ in the limit $l \to +\infty$. It is important that in the limit $l \to +\infty$ the energies G of all polydomain states "split" into two levels—the ground domain state "0" with $G_0 = -G_b$ and the excited state "1" with $G_1 = -\frac{G_b}{2}$, which are separated by the "gap" of width $\Delta G = \frac{G_b}{2}$. Each of these two levels splits on the infinite set of sublevels, which are characterized by a multiple close-energy polydomain morphologies with number $\{0, N_y\}$ and $\{N_x, N_y\}$ ($N_{x,y} \geqslant 1$), respectively.

The two-level energy structure of the polydomain states for $\lambda_i = 0$ principally differs from the single level existing in the case $\lambda_i \to +\infty$ [compare Figs. 5(a) and 6(a)]. Since zero polarization at the film surfaces can be realized experimentally by creation of the ultrathin nonferroelectric passive layers at the surfaces [63], this suggests possible strategies to switch the polarization state between the sublevels 0 and 1. Imagine that we have excited (e.g., by electric field) the film polarization to the one of the polydomain states 1. When the system is released, it tries to thermalize its energy excess, and, if the dissipation is very small in a film without imperfections [i.e., $\rho \gg \tau^2$ in Eqs. (6)], it can oscillate with some period between the excited states 1 and ground state 0.

It is seen from Figs. 6(b)–6(g) that the profile and amplitude of the polydomain solution (13) is determined by the film thickness l and by the "nodes" pair $\{N_x, N_y\}$, but the details of domain pattern slightly differ from the ones shown in Figs. 5(b)–5(g). Simple Ising-type domains with a quasisinusoidal profile for l slightly bigger than l_{cr} [see Figs. 6(b)], or with strongly anharmonic "snoidal" profile for $l \gg l_{cr}$

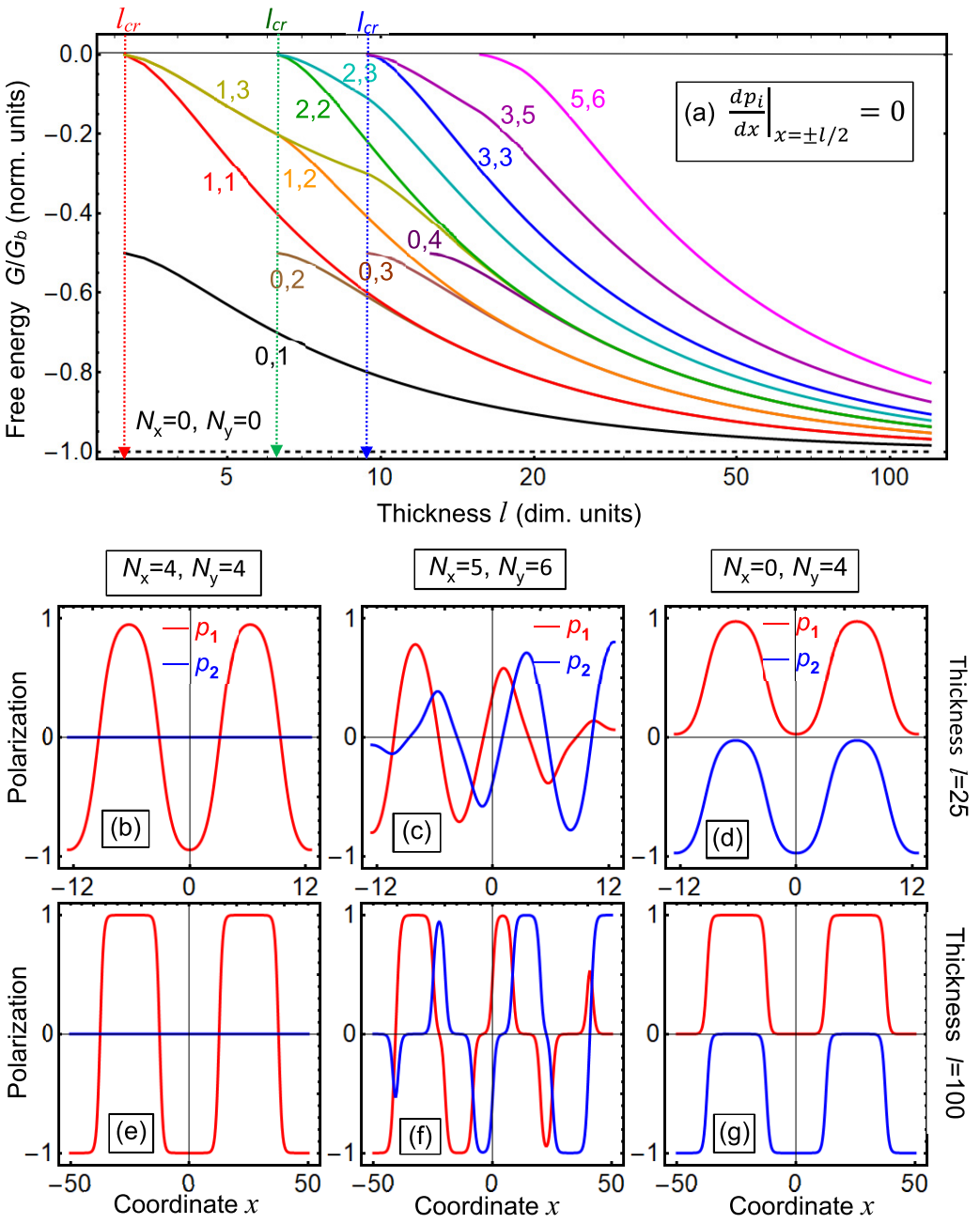

FIG. 5. (a) Energy of the metastable polydomain states as a function of dimensionless film thickness l for different numbers of domain walls inside the film, $\{N_x, N_y\}$, denoted near the curves. (b)–(g) Distribution of polarization components, p_1 (red curves) and p_2 (blue curves), in the film of thickness $l = 25$ (b)–(d) and $l = 100$ (e)–(g) calculated using Eqs. (13) for different numbers $N_x = 4$ and $N_y = 4$ (b),(e); $N_x = 5$ and $N_y = 6$ (c),(f); $N_x = 0$ and $N_y = 4$ (d),(g). The absolutely stable single-domain state with $N_x = N_y = 0$ is shown for comparison by a dashed line. Natural boundary conditions are used for polarization components: $\frac{dp_i}{dx}|_{x=\pm l/2} = 0$, i.e., $\lambda_i \to +\infty$ for all plots (a)–(g). Ferroelectric anisotropy factor $\mu = 3$, and energy scale factor $G_b = 1/4$.

[see Fig. 6(e)], correspond to the same numbers $N_x = N_y$. Rather complex phase-shifted asymmetric Bloch-Ising-type profiles, which are quasiharmonic for $l \approx l_{cr}$ [see Fig. 6(c)], or strongly anharmonic for $l \gg l_{cr}$ [see Fig. 6(f)], correspond to the close numbers $N_x = N_y - 1$. Simple antiphase [i.e., $p_1(x) = -p_2(x)$] and antisymmetric [$p_{1,2}(x) = -p_{1,2}(-x)$] Bloch-Ising type profiles, which are quasiharmonic for $l \approx l_{cr}$ [see Fig. 6(d)], and strongly anharmonic for $l \gg l_{cr}$ [see Fig. 6(g)], correspond to the pairs $\{0, N_y\}$ or $\{N_x, 0\}$.

To resume the analysis of the limiting cases $\lambda_i \to \infty$ and $\lambda_i = 0$, analytical solutions (13), which contain four free parameters (m, n, x_{w1}, and x_{w2}), are suitable candidates for a general equilibrium solution of nonlinear differential EL equations (6) for $\mu = 3$, since the number of free parameters is enough to satisfy arbitrary boundary conditions (7) at the film surfaces. The solutions (13) are degenerated for a fixed boundary condition, because they contain different numbers of domain walls proportional to N_x for $p_1 + p_2$ and to N_y for

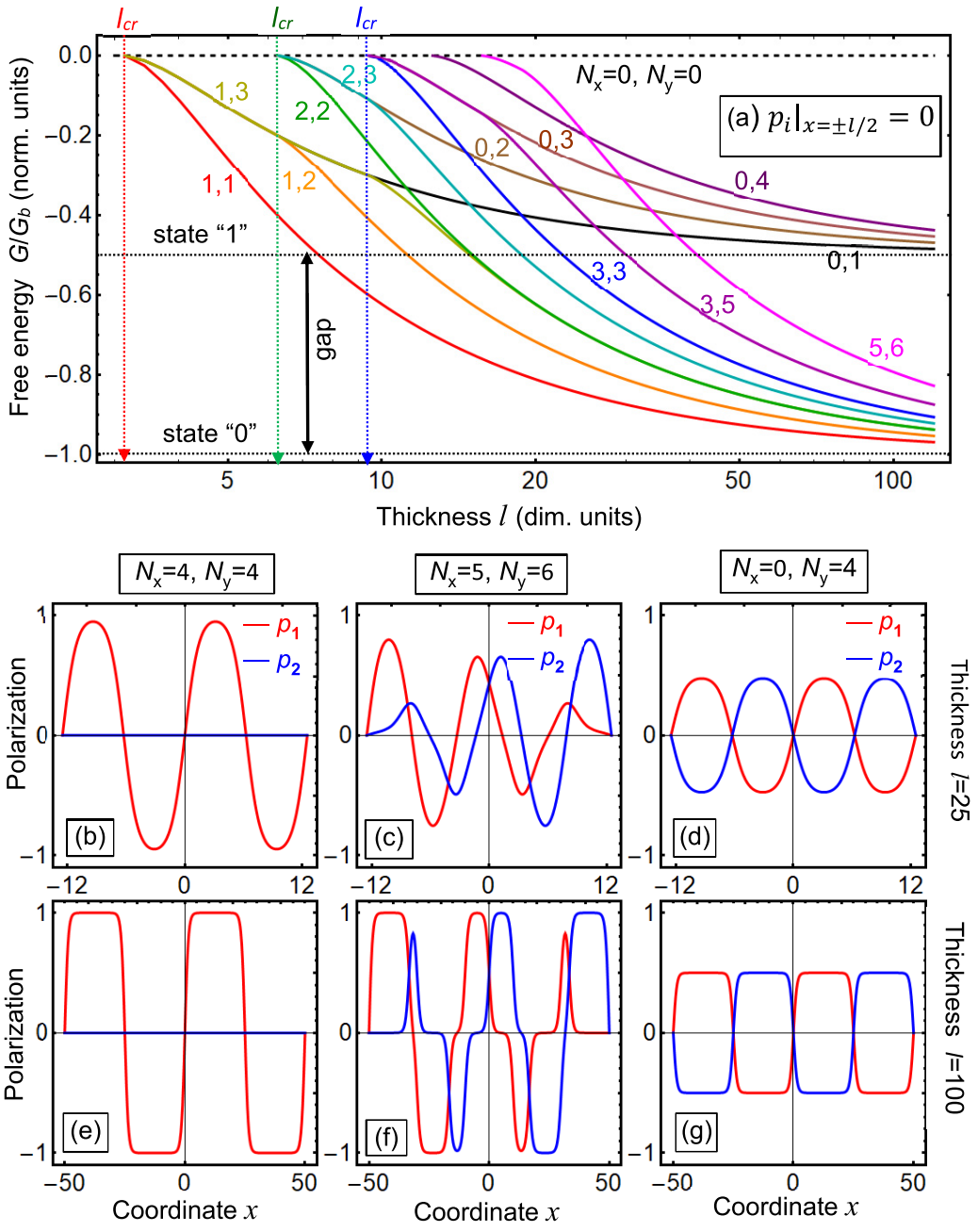

FIG. 6. (a) Energy of the polydomain states as a function of dimensionless film thickness l for different numbers of domain walls inside the film, $\{N_x, N_y\}$, denoted near the curves. (b)–(g) Distribution of polarization components, p_1 (red curves) and p_2 (blue curves), in the film of thickness $l = 25$ (b)–(d) and $l = 100$ (e)–(g) calculated using Eqs. (13) for different numbers $N_x = 4$ and $N_y = 4$ (b),(e); $N_x = 5$ and $N_y = 6$ (c),(f); $N_x = 0$ and $N_y = 4$ (d),(g). The unstable single-domain state with $N_x = N_y = 0$ is shown for comparison by a dashed line. Ferroelectric anisotropy factor $\mu = 3$, and $G_b = 1/4$. Zero boundary conditions are used for polarization components, $p_i|_{x=\pm l/2} = 0$, i.e., $\lambda_i = 0$ for all plots (a)–(g).

$p_1 - p_2$. The analysis of the free energy (15) dependence on the number of domains for a fixed film thickness l allows us to select the single- or polydomain solution corresponding to the minimal energy [see Figs. 5(a) and 6(a)]. We obtained that the single-domain state corresponds to the minimal energy for the case of zero polarization derivative at the film surfaces [namely for $\lambda_i \to \infty$ in Eq. (7b)], while the Ising-Bloch polydomain states with the total number of rotational domain walls $N_x + N_y \geqslant 1$ minimize the system energy for zero polarization at the film surfaces [namely for $\lambda_i = 0$ in Eq. (7b)]. In the case $\lambda_i = 0$ the energy of polydomain states splits into two levels 0 and 1, and each of the levels is the great number of the close-energy sublevels (infinite in the limit $l \to \infty$), whose domain structure is characterized by the pair of nodes $\{0, N_y\}$ for the level 1 and $\{N_x, N_y\}$ for the level 0, where $N_{x,y} \geqslant 1$.

2. Periodic-antiperiodic conditions for the polarization components

If the periodic-antiperiodic conditions (7c) are valid for two components of polarization, one can put $m = n$ and $x_{w1} = -x_{w2} = x_w$ in the solution (13), while it is not the only possibility in the case. Anyway, the two parameters, m and x_w, remained undefined from Eqs. (13) in the case of Eqs. (7c). The free energy G is minimal for $m \to 1$ and $n \to 1$ corresponding to a solitary domain wall. In the simultaneous limit $m = n \to 1$ the solution (13) transforms into a solitary wall solution (9), namely $p_1(x_3) = \frac{1}{2}[\tanh(\frac{x+x_w}{\sqrt{2}}) + \tanh(\frac{x-x_w}{\sqrt{2}})]$ and $p_2(x_3) = \frac{1}{2}[\tanh(\frac{x+x_w}{\sqrt{2}}) - \tanh(\frac{x-x_w}{\sqrt{2}})]$. These expressions become identical with Ivanchik solution [43] after elementary calculations (see Appendix A in the Supplemental Material [62] for details).

The solution (13) can be considered as a trial function for $-1 < \mu < 3$. For instance, in the case of the boundary conditions (7c) the trial functions for polydomain solutions are

$$p_1(x) = a_1 + \frac{b_1}{2}\sqrt{\frac{2m}{1+m}}\left[\mathrm{sn}\left(\frac{x+x_w}{\sqrt{1+m}}\middle|m\right) + \mathrm{sn}\left(\frac{x-x_w}{\sqrt{1+m}}\middle|m\right)\right], \tag{17a}$$

$$p_2(x) = a_2 + \frac{b_2}{2}\frac{w}{x_w}\sqrt{\frac{2m}{1+m}}\left[\mathrm{sn}\left(\frac{x+x_w}{\sqrt{1+m}}\middle|m\right) - \mathrm{sn}\left(\frac{x-x_w}{\sqrt{1+m}}\middle|m\right)\right], \tag{17b}$$

where "free" parameters, constant offsets a_i and amplitudes b_i, are introduced in the same way as in Eqs. (9). They should be determined by using the direct variational method similarly to the case of a solitary domain wall considered in the previous Sec. III.

B. Analytical solutions for the Ising polydomains

For the case of high positive ferroelectric anisotropy $\mu > 3$ the stable polydomain solution of Eqs. (6a) becomes of Ising type and μ independent, since the p_2 component is absent. The corresponding polarization profile has the snoidal form:

$$p_1(x_3) = \sqrt{\frac{2m}{1+m}}\,\mathrm{sn}\left(\frac{x+x_w}{\sqrt{1+m}}\middle|m\right), \quad p_2(x_3) \equiv 0. \tag{18a}$$

The snoid modulus m and shift x_w should be determined from the boundary conditions (7). For the two limiting cases, $\lambda_i = 0$ and $\lambda_i \to +\infty$, the modulus m satisfies the condition $2N\sqrt{1+m}\,\mathbf{K}(m) = l$, where the integer number N regulates the number of solution "nodes" [compare with Eqs. (14a)]. The shift $x_w = \frac{l}{2}(1 \pm \frac{1}{N})$ for $\lambda_i \to +\infty$, or $x_w = \frac{l}{2}(1 \pm \frac{1-(-1)^s}{N})$ for $\lambda_i = 0$ [compare with Eqs. (14b) and (14c)]. Using the solution (18a), the free energy was derived as

$$G[m] = \frac{1}{l}\int_{-\frac{l}{2}}^{\frac{l}{2}} dx\left[-\frac{p^2}{2} + \frac{p^4}{4} + \frac{1}{2}\left(\frac{dp}{dx}\right)^2\right] \equiv -\frac{1}{3(1+m)^2}\left(2 + m - 2(1+m)\frac{\mathbf{E}(m)}{\mathbf{K}(m)}\right). \tag{18b}$$

The first integral is $I(m) = -\frac{m}{(1+m)^2}$. As it can be seen, Eqs. (18) are the particular case of Eqs. (13)–(15) for the case $N_x = N_y = N$. Thus, the solutions (18a) and their energy (18b) are presented among other curves with $N_x = N_y$, which are shown in Figs. 5 and 6. To resume, the analytical polydomain solution (18a), which contains two free parameters (m and x_{w2}), is a suitable candidate for a general stable solution of EL equations (6) for $\mu > 3$, since the number of free parameters is enough to satisfy the boundary conditions (7) at the film surfaces. The solution (18) is degenerated for a fixed boundary condition, because it contains a different number of domains (N or $N + 1$). The analysis of the free energy (18b) dependence on the number of domains for a fixed film thickness l allows us to select the single- or polydomain solution corresponding to the minimal energy [see curves {1, 1}, {2, 2}, and {3, 3} in Figs. 5(a) and 6(a)]. The single-domain state corresponds to the minimal energy for the case of polarization zero derivative at the surface [namely for $\lambda_i \to \infty$ in Eq. (7b)], while the Ising polydomains minimize the system energy for, e.g., zero polarization at the surface [namely for $\lambda_i \to 0$ in Eq. (7b)].

V. POSSIBLE APPLICATIONS OF ANALYTICAL RESULTS FOR BAYESIAN ANALYSIS AND INFORMATION PROCESSING

A. Bayesian analysis of domain-wall profiles

Let us consider a model situation when we know the ferroelectric film thickness L, the temperature T is fixed, and most of the ferroelectric material parameters in Eqs. (1) are determined from independent experiments, or tabulated. For instance, the parameters a_i, a_{ii}, and a_{ij} can be determined from the measurements of dielectric permittivity and spontaneous polarization temperature dependencies in a bulk homogeneous ferroelectric [5,6]. Much more complex is to determine the gradient coefficients g_{ijkl}, and the error originated from g_{ijkl} estimation using the intrinsic width of differently oriented uncharged domain walls [5,6] is typically high (~50–100%) due to wall pinning and "trembling" near lattice defects and other imperfections. Moreover, the direct determination of extrapolation lengths λ_i, introduced in Eq. (7b), is a true challenge, because the surface energy coefficients a_i^S in Eq. (1b) depend on the surface/interface chemistry and surface defects in a prior unknown way, and only indirect estimates have been done for several particular cases [46]. The only exception may be the deposition of artificial dead layers [63] at the film surfaces, which yield $p_i(\pm l/2) = 0$ and so $\lambda_i = 0$. Hence, the dimensionless control parameter μ can be regarded known for a fixed temperature, while the dimensionless extrapolation and correlation lengths, $\lambda_i \cong \frac{g_{44}R_c}{a_i^S}$ and $R_c \cong \sqrt{g_{44}/|2a_1|}$, are *prior* unknown.

In the previous section we calculated the energy levels $G[m, n]$ given by Eqs. (15). The redefinition $G[m, n] \equiv G(N_x, N_y)$ is possible, since the relation between the pair of modules $\{m, n\}$ and integers $\{N_x, N_y\}$ determining the domain numbers is established by, e.g., Eq. (14a) for $\mu = 3$ in particular cases $\lambda_i \to +\infty$ and $\lambda_i \to 0$. Since these results can be extended for the case of arbitrary $\mu > -1$ by application of direct variational method, as described above, we can

assume that the energy levels describing different polarization states $p_i(x, N_x, N_y, R_c,\ \lambda)$, the expected (i.e., averaged over all realizations) polarization state $\langle p_i(x, R_c,\ \lambda),\rangle$ and energy $G(R_c,\ \lambda)$ can be calculated for the *posterior* known sets of parameters $\lambda = \{\lambda_i\}$ and R_c. Namely

$$\langle p_i(x, R_c,\ \lambda)\rangle = \sum_{N_{x,y}=0}^{N_{x,y}=N_m} p_i(x, N_x, N_y, R_c,\ \lambda) W[N_x, N_y|R_c,\ \lambda], \tag{19a}$$

$$\langle G(R_c,\ \lambda)\rangle = \sum_{N_{x,y}=0}^{N_{x,y}=N_m} G(N_x, N_y, R_c,\ \lambda) W[N_x, N_y|R_c,\ \lambda], \tag{19b}$$

where $i = 1, 2$, and we introduced the designation $\lambda = \{\lambda_i\}$ for the sake of brevity. The maximal number of the energy states N_m is defined from the condition $N_m = \mathrm{Trunc}[\frac{l}{\pi}]$, obtained from Eq. (16) for $l_{\mathrm{cr}}(N_m)$. For example, $N_m = 6$ for $l = 20$ [see Figs. 5(a) and 6(a)].

The conditional prior probability $W[N_x, N_y|g,\ \lambda]$ of the state $p_i(x, N_x, N_y, R_c,\ \lambda)$ realization under the validity of "event"—realization of the parameters $\{R_c,\ \lambda\}$ in the film—is expressed via the energy levels $G(N_x, N_y, R_c,\ \lambda)$ and canonic statistic sum $Z(g,\ \lambda)$ in a conventional way:

$$W[N_x, N_y|R_c,\ \lambda] = \frac{k_{N_{x,y}}}{Z(R_c,\ \lambda)} \exp\left[-\frac{G(N_x, N_y, R_c,\ \lambda)}{k_B T}\right], \tag{19c}$$

$$Z(R_c,\ \lambda) = \sum_{N_{x,y}=0}^{N_{x,y}=N_m} G(N_x, N_y, R_c,\ \lambda). \tag{19d}$$

Here the statistical weight $k_{N_{x,y}}$ the of the state $p_i(x, N_x, N_y, R_c,\ \lambda\ )$ is equal to 2 (when degeneration $p_1 \to -p_1$ exists) or 4 (when degeneration $p_1 \to \pm p_2$ exists) depending on μ value.

Using the Bayesian approach described in Refs. [58,59], we can determine the posterior conditional probability $W[R_c,\ \lambda|N_x, N_y]$ of the $\{R_c,\ \lambda\}$ parameters:

$$W[R_c,\ \lambda|N_x, N_y] = \frac{W[N_x, N_y|\ R_c, \lambda]}{W[N_x, N_y]} W[R_c,\ \lambda], \tag{20a}$$

where the "marginal" or "unconditional" probability $W[N_x, N_y]$ of the state $p_i(x, N_x, N_y\ )$ realization is the sum and/or integral over all prior probabilities $W[R_c,\ \lambda]$ of the $\{R_c,\ \lambda\}$ events:

$$W[N_x, N_y] = \int_{R_{\min}}^{R_{\max}} dR_c \int_0^{\infty} d\lambda\ W[R_c,\ \lambda] W[N_x, N_y|\ R_c, \lambda]. \tag{20b}$$

In practice one can determine the probability $W[N_x, N_y]$ by the fitting of analytical profiles (17) to the domain-wall profiles, which are measured experimentally. Thus, expressions (20) illustrate that the energies (15), corresponding to the analytical solutions (13) or (17), and statistical probabilities (19) can be used for a Bayesian analysis of domain-wall profiles reconstructed from atomic displacements measured by HR STEM in thin ferroelectric films (see Refs. [58,59]).

As a toy model, let us assume that R_c is determined reliably from the intrinsic width of domain walls, and consider only two possible and equiprobable events, $\lambda = +\infty$ and $\lambda = 0$. Under these conditions, Eqs. (20) acquire much simpler form:

$$W[\lambda|N_x, N_y] \cong \frac{W[N_x, N_y|\ \lambda]}{W[N_x, N_y|\ 0] + W[N_x, N_y|\ \infty]}, \tag{21a}$$

where $\lambda = +\infty$ or $\lambda = 0$.

Alternatively, when all λ values can be regarded quasiequiprobable in the region $\{0,\ \lambda_{\max}\}$, we can put $W[R_c,\ \lambda] \approx \frac{1}{\lambda_{\max}}$ and simplify Eqs. (20) as follows:

$$W[\lambda|N_x, N_y] \cong \frac{W[N_x, N_y|\ \lambda]}{\int_0^{\lambda_{\max}} d\lambda\ W[N_x, N_y|\ \lambda]}. \tag{21b}$$

Expressions (21) demonstrate that the Bayes formula allows us to estimate the posterior probability of different λ values realization, since the posterior probability is proportional to the prior one. The treelike diagram illustrating the application of the Bayes formula for Eqs. (21) is shown in Fig. 7. The diagram demonstrates possible paths between the prior guess for extrapolation length ($\lambda = 0$ or $\lambda = \infty$) and posterior measurement of the domain state corresponding to the sublevels 0 with domain numbers $\boldsymbol{L}_0 = \{N_x, N_y\}$, or sublevels 1 with domain numbers $\boldsymbol{L}_1 = \{0, N_y\} \cup \{N_x, 0\}$, where $N_{x,y} \geqslant 1$ [see Figs. 5(a) and 6(a) for details].

B. Information processing

Let us consider a rather thick ferroelectric film ($l \gg 100$) with zero polarization at its surfaces ($p_i|_{x=\pm l/2} = 0$), whose versatile domain morphology is determined by the maximal number of domain walls $N_m \gg 1$, where N_m is defined from the condition $N_m = \mathrm{Trunc}[\frac{l}{\pi}]$. The corresponding energy structure is similar to the right part of the two-level system shown in Fig. 6(a), at that the level 1 is divided on $2N_m$ sublevels with a node structure $\{0, N_y\} \cup \{N_x, 0\}$, and the level 0 is divided on N_m^2 sublevels with a node structure $\{N_x, N_y\}$, where $N_{x,y} \geqslant 1$. The energies of sublevels 1 are very close to $G_1 = -1/2$, and the energies of all sublevels 0 are very close to $G_0 = -1$ (in G_b units). "Very close" means that the energy difference between the sublevels $\Delta G_{x,y}$ is smaller than thermal fluctuations energy $k_B T$, and decreases with l increase, so that each of the complex levels 0 and 1 presents itself a great number of polarization states, which are almost indistinguishable at $k_B T \geqslant \Delta G_{x,y}$. However, since each sublevel is characterized by a different number (and often configuration) of domain walls, the two-level system can be considered as a very big multibit that potentially can imitate a quantum bit (q-bit) better the larger the number N_m.

Let us imagine that we initially excite the film polarization to the one of the $2N_m$ polydomain states 1. When the system is released, it tries to thermalize its energy excess, and, if the dissipation is very small in a film without imperfections [i.e., $\rho \gg \tau^2$ in Eqs. (6)], it can oscillate with some period between the excited states 1 and the ground states 0. Since each level has a great number of sublevels, the oscillations between the levels can be used for, e.g., racetrack memory and q-bit operation imitation, which utilizes the parallelism of the polarization states evolution.

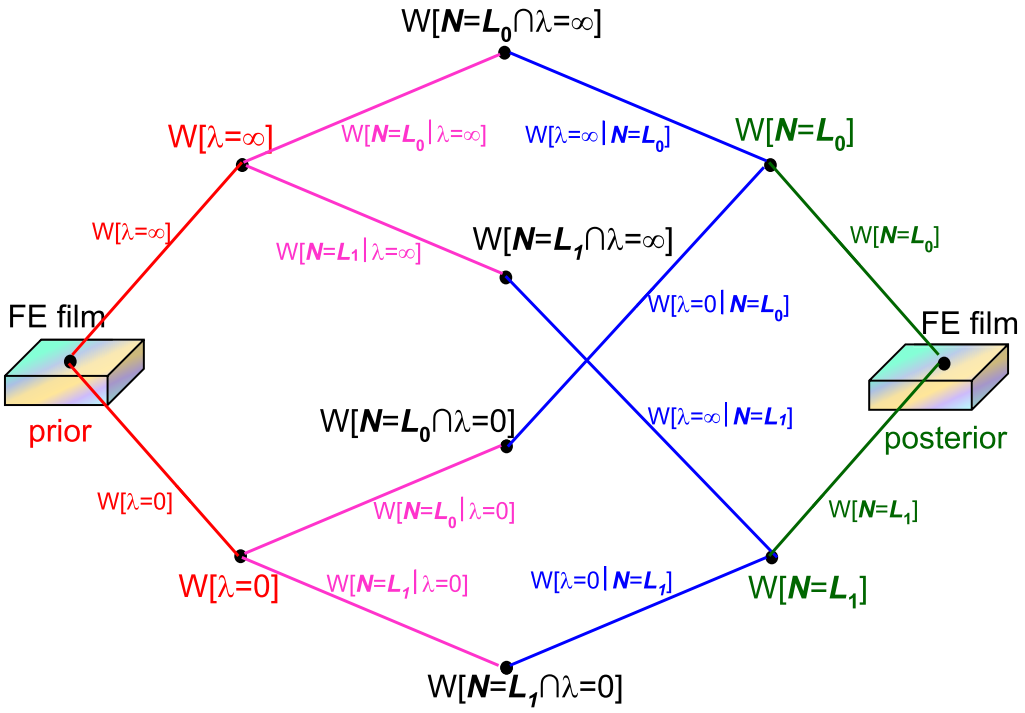

FIG. 7. The treelike diagram illustrating the Bayes formula for Eqs. (21), where we introduce the domain number $\boldsymbol{N} = \{N_x, N_y\}$, and the designations for domain structure of the energy levels 0 and 1, $\boldsymbol{L}_0 = \{N_x, N_y\}$ and $\boldsymbol{L}_1 = \{0, N_y\} \cup \{N_x, 0\}$, respectively ($N_{x,y} \geqslant 1$). Other designations: W[A] is a probability of the event A, W[B|A] is the probability of event B under the condition A, and W[A∩B] is a mutual probability of event AB. All paths between the prior guess for extrapolation length ($\lambda = 0$ or $\lambda = \infty$) and posterior measurement of domain numbers ($\boldsymbol{N} = \boldsymbol{L}_0$ or $\boldsymbol{N} = \boldsymbol{L}_1$) illustrate the symmetry of Bayes formula $W[B|A]\,W[A] = W[A \cap B] = W[A|B]\,W[B\,]$.

To elaborate on the idea, we preliminarily study the oscillatory dynamic of domain structure under the absence and in the presence of losses, for initial seeding in the form of a random polarization distribution and for the boundary condition $p_i|_{x=\pm l/2} = 0$. We obtained that in some cases the polarization vector oscillates (with or without damping in dependence on the loss factor τ) between several metastable domain states, without smearing to all available states. This result can be considered as the direct demonstration of the Fermi-Pasta-Ulam-Tsingou (FPUT) paradox [64] (other names are FPU problem or recurrence [65]), which states that the energy in a weakly coupled nonlinear system avoids thermalization and travels between the available modes of the system without diffusing to all available modes.

VI. SUMMARY

We considered the dynamics of a 180° uncharged rotational domain wall in a multiaxial ferroelectric film within the framework of the analytical LGD approach. FEM was used to solve numerically the system of the coupled nonlinear EL differential equations of the second order for two components of polarization. It appeared that the static wall structure (e.g., Ising, Ising-Bloch, or mixed type) and corresponding (meta)stable phase of the film are dependent on the single control parameter—dimensionless factor of ferroelectric anisotropy μ, that can vary in a continuous range $-1 < \mu$. Using spline interpolations, we fitted the static profile of a solitary domain wall, calculated by FEM, with multiparametric hyperbolic kinklike functions for the two-component polarization, and extracted the five μ-dependent parameters from the fitting to FEM curves. The surprisingly high accuracy of the fitting results in the entire range $-1 < \mu < 5$, allows us to conclude that the analytical functions, which are trial functions in the direct variational method, can be treated as the high-accuracy variational solution of the static EL equations with cubic nonlinearity.

Next, using the LGD approach, we derived and analyzed the two-component and one-component analytical solutions of the static EL equations for a polydomain 180° domain structure in a multiaxial ferroelectric film. The analytical solutions in the form of elliptic Jacobi functions, which contain two and four free parameters, respectively, are suitable candidates for a general stable solution of EL equations, since the number of free parameters is enough to satisfy the wide class of boundary conditions at the film surfaces. The solutions are degenerate for definite boundary conditions, because they can contain a different number of domains for p_1 and p_2 components. However, the analysis of the free-energy dependence on the number of domains for a fixed film thickness allowed us to select those single- or polydomain analytical solutions which correspond to the minimal energy. In particular, we obtained that the single-domain state corresponds to the minimal energy for the case of the polarization zero derivative at the film surfaces, while the solution with Ising-Bloch domain walls minimizes the system energy for zero polarization at the film surfaces. The analytical solutions can become a useful tool for Bayesian analysis of domain-wall profiles reconstructed from

atomic displacements measured by HR STEM in ferroelectric films [58,59].

For thick films with zero polarization at the surfaces the energy of the polydomain states split into two levels 0 and 1. Each of the levels 0 or 1 contains a large number of the close-energy sublevels, whose domain morphology is characterized by different structure of nodes for the two-component polarization $\boldsymbol{p} = \{p_1,\ p_2\}$, namely $\{0, N_y\}$ for level 1 and $\{N_x, N_y\}$ for the level 0, where $1 \leqslant N_{x,y} \leqslant N_m$ and $N_m \gg 1$. Since zero polarization at the surface can be realized experimentally relatively easily by creation of subsurface nonferroelectric passive layers, one can switch the polarization state between levels 0 and 1. Under certain favorable conditions, the two-level system can oscillate with some period between the excited states 1 and ground state 0, and the oscillations can be used for, e.g., racetrack memory and q-bit operation imitation.

The Department of Energy will provide public access to these results of federally sponsored research in accordance with the DOE Public Access Plan [66].

ACKNOWLEDGMENTS

Authors gratefully acknowledge B. G. Sumpter (ORNL) for useful suggestions and improvements of the manuscript. Authors are very grateful to the referees for useful remarks and stimulating discussions. This effort (S.V.K.) is based upon work supported by the US Department of Energy (DOE), Office of Science, Basic Energy Sciences (BES), Materials Sciences and Engineering Division and was performed at the Oak Ridge National Laboratorys Center for Nanophase Materials Sciences (CNMS), a US Department of Energy, Office of Science User Facility. A.N.M. acknowledges the Target Program of Basic Research of the National Academy of Sciences of Ukraine "Prospective basic research and innovative development of nanomaterials and nanotechnologies for 2020 - 2024", Project No. 1/20-M (state registration number 0120U102306).

A.N.M. and S.V.K. generated the research idea, stated the problem, and wrote the manuscript. A.N.M. and E.A.E. performed analytical calculations. E.A.E. and Y.M.F. wrote the codes and performed numerical calculations.

[1] S. V. Kalinin, A. N. Morozovska, L. Q. Chen, and B. J. Rodriguez, Local polarization dynamics in ferroelectric materials, Rep. Prog. Phys. **73**, 056502 (2010).

[2] P. Maksymovych, A. N. Morozovska, P. Yu, E. A. Eliseev, Y.-H. Chu, R. Ramesh, A. P. Baddorf, and S. V. Kalinin, Tunable metallic conductance in ferroelectric nanodomains, Nano Letters **12**, 209 (2012).

[3] Y. L. Tang, Y. L. Zhu, X. L. Ma, A. Y. Borisevich, A. N. Morozovska, E. A. Eliseev, W. Y. Wang, Y. J. Wang, Y. B. Xu, Z. D. Zhang, and S. J. Pennycook, Observation of a periodic array of flux-closure quadrants in strained ferroelectric $PbTiO_3$ films, Science **348**, 547 (2015).

[4] M. J. Han, Y. J. Wang, D. S. Ma, Y. L. Zhu, Y. L. Tang, Y. Liu, N. B. Zhang, J. Y. Ma, and X. L. Ma, Coexistence of rhombohedral and orthorhombic phases in ultrathin $BiFeO_3$ films driven by interfacial oxygen octahedral coupling, Acta Mater. **145**, 220 (2018).

[5] A. S. Sidorkin, *Domain Structure in Ferroelectrics and Related Materials* (Cambridge International Science, Cambridge, 2006).

[6] A. K. Tagantsev, L. E. Cross, and J. Fousek, *Domains in Ferroic Crystals and Thin Films* (Springer, Dordrecht, 2010).

[7] S. Cherifi-Hertel, H. Bulou, R. Hertel, G. Taupier, K. D. H. Dorkenoo, C. Andreas, J. Guyonnet, I. Gaponenko, K. Gallo, and P. Paruch, Non-ising and chiral ferroelectric domain walls revealed by nonlinear optical microscopy, Nat. Commun. **8**, 15768 (2017).

[8] E. A. Eliseev, Y. M. Fomichov, S. V. Kalinin, Y. M. Vysochanskii, P. Maksymovich, and A. N. Morozovska, Labyrinthine domains in ferroelectric nanoparticles: Manifestation of a gradient-induced morphological phase transition, Phys. Rev. B **98**, 054101 (2018).

[9] M. J. Han, E. A. Eliseev, A. N. Morozovska, Y. L. Zhu, Y. L. Tang, Y. J. Wang, X. W. Guo, and X. L. Ma, Mapping gradient-driven morphological phase transition at the conductive domain walls of strained multiferroic films, Phys. Rev. B **100**, 104109 (2019).

[10] Y. Nahas, S. Prokhorenko, J. Fischer, B. Xu, C. Carrétéro, S. Prosandeev, M. Bibes, S. Fusil, B. Dkhil, V. Garcia, and L. Bellaiche, Inverse transition of labyrinthine domain patterns in ferroelectric thin films, Nature (London) **577**, 47 (2020).

[11] A. N. Morozovska, Y. M. Fomichov, P. Maksymovych, Y. M. Vysochanskii, and E. A. Eliseev, Analytical description of domain morphology and phase diagrams of ferroelectric nanoparticles, Acta Mater. **160**, 109 (2018).

[12] J. Hlinka and P. Ondrejkovic, Skyrmions in ferroelectric materials, in *Solid State Physics* (Academic, New York, 2019), Vol. 70, pp. 143–169.

[13] *Ferroelectric Materials for Energy Applications*, edited by H. Huang and J. F. Scott (Wiley-VCH, Weinheim, 2018).

[14] J. Ouyang, *Nanostructures in Ferroelectric Films for Energy Applications: Domains, Grains, Interfaces and Engineering Methods* (Elsevier, New York, 2019).

[15] D. Damjanovic, Ferroelectric, dielectric and piezoelectric properties of ferroelectric thin films and ceramics, Rep. Prog. Phys. **61**, 1267 (1998).

[16] T. M. Shaw, S. Trolier-McKinstry, and P. C. McIntyre, The properties of ferroelectric films at small dimensions, Annu. Rev. Mater. Sci. **30**, 263 (2000).

[17] N. Setter, D. Damjanovic, L. Eng, G. Fox, S. Gevorgian, S. Hong, A. Kingon, H. Kohlstedt, N. Y. Park, G. B. Stephenson, I. Stolitchnov, A. K. Tagantsev, D. V. Taylor, T. Yamada, and S. Streiffer, Ferroelectric thin films: Review of materials, properties, and applications, J. Appl. Phys. **100**, 051606 (2006).

[18] J.-J. Wang, B. Wang, and L.-Q. Chen, Understanding, predicting, and designing ferroelectric domain structures and switching guided by the phase-field method, Annu. Rev. Mater. Res. **49**, 127 (2019).

[19] A. N. Morozovska, E. A. Eliseev, Y. M. Fomichov, Yu. M. Vysochanskii, V. Yu. Reshetnyak, and D. R. Evans, Controlling

the domain structure of ferroelectric nanoparticles using tunable shells, Acta Mater. **183**, 36 (2020).

[20] A. N. Morozovska, E. A. Eliseev, R. Hertel, Y. M. Fomichov, V. Tulaidan, V. Yu. Reshetnyak, and D. R. Evans, Electric field control of three-dimensional vortex states in core-shell ferroelectric nanoparticles, Acta Mater. **200**, 256 (2020).

[21] A. N. Morozovska, E. A. Eliseev, D. Chen, V. Shvetz, C. T. Nelson, and S. V. Kalinin, Melting of spatially modulated phases in la-doped $BiFeO_3$ at surfaces and surface-domain wall junctions, Phys. Rev. B **102**, 075426 (2020).

[22] P. Marton, Discretisation originated Peierls–Nabarro barriers in simulations of ferroelectrics, Phase Transit. **91**, 959 (2018).

[23] S. Jesse, B. J. Rodriguez, S. Choudhury, A. P. Baddorf, I. Vrejoiu, D. Hesse, M. Alexe, E. A. Eliseev, A. N. Morozovska, J. Zhang, L.-Q. Chen, and S. Kalinin, Direct imaging of the spatial and energy distribution of nucleation centres in ferroelectric materials, Nat. Mater. **7**, 209 (2008).

[24] S. Zhukov, Y. A. Genenko, O. Hirsch, J. Glaum, T. Granzow, and H. von Seggern, Dynamics of polarization reversal in virgin and fatigued ferroelectric ceramics by inhomogeneous field mechanism, Phys. Rev. B **82**, 014109 (2010).

[25] Y. A. Genenko, S. Zhukov, S. V. Yampolskii, J. Schütrumpf, R. Dittmer, W. Jo, H. Kungl, M. J. Hoffmann, and H. von Seggern, Universal polarization switching behavior of disordered ferroelectrics, Adv. Funct. Mater. **22**, 2058 (2012).

[26] M. J. Highland, T. T. Fister, D. D. Fong, P. H. Fuoss, C. Thompson, J. A. Eastman, S. K. Streiffer, and G. B. Stephenson, Equilibrium Polarization of Ultrathin $PbTiO_3$ with Surface Compensation Controlled by Oxygen Partial Pressure, Phys. Rev. Lett. **107**, 187602 (2011).

[27] I. S. Vorotiahin, A. N. Morozovska, and Y. A. Genenko, Hierarchy of domain reconstruction processes due to charged defect migration in acceptor doped ferroelectrics, Acta Mater. **184**, 267 (2020).

[28] D. A. Freedman, D. Roundy, and T. A. Arias, Elastic effects of vacancies in strontium titanate: Short- and long-range strain fields, elastic dipole tensors, and chemical strain, Phys. Rev. B **80**, 064108 (2009).

[29] Ivan S. Vorotiahin, Eugene A. Eliseev, Qian Li, Sergei V. Kalinin, Yuri A. Genenko, and Anna N. Morozovska, Tuning the polar states of ferroelectric films via surface charges and flexoelectricity, Acta Mater. **137**, 85 (2017).

[30] E. A. Eliseev, I. S. Vorotiahin, Y. M. Fomichov, M. D. Glinchuk, S. V. Kalinin, Y. A. Genenko, and A. N. Morozovska, Defect driven flexo-chemical coupling in thin ferroelectric films, Phys. Rev. B **97**, 024102 (2018).

[31] D. Alikin, Y. Fomichov, S. P. Reis, A. Abramov, D. Chezganov, V. Shur, E. Eliseev, A. Morozovska, E. Araujo, and A. Kholkin, Polarization-dependent conductivity of grain boundaries in $BiFeO_3$ thin films, Appl. Mater. Today **20**, 100740 (2020).

[32] S. Zhang, X. Guo, Y. Tang, D. Ma, Y. Zhu, Y. Wang, S. Li, M. Han, D. Chen, J. Ma, B. Wu, and X. Ma, Polarization rotation in ultrathin ferroelectrics tailored by interfacial oxygen octahedral coupling, ACS Nano **12**, 3681 (2018).

[33] S. V. Kalinin, Y. Kim, D. Fong, and A. N. Morozovska, Surface-screening mechanisms in ferroelectric thin films and their effect on polarization dynamics and domain structures, Rep. Prog. Phys. **81**, 036502 (2018).

[34] J. Junquera and P. Ghosez, Critical thickness for ferroelectricity in perovskite ultrathin films, Nature (London) **422**, 506 (2003).

[35] A. K. Tagantsev, G. Gerra, and N. Setter, Short-range and long-range contributions to the size effect in metal-ferroelectric-metal heterostructures, Phys. Rev. B **77**, 174111 (2008).

[36] E. A. Eliseev and A. N. Morozovska, General approach to the description of the size effect in ferroelectric nanosystems, J. Mater. Sci. **44**, 5149 (2009).

[37] V. Stepkova, P. Marton, and J. Hlinka, Stress-induced phase transition in ferroelectric domain walls of $BaTiO_3$, J. Phys.: Condens. Matter **24**, 212201 (2012).

[38] M. Taherinejad, D. Vanderbilt, P. Marton, V. Stepkova, and J. Hlinka, Bloch-type domain walls in rhombohedral $BaTiO_3$, Phys. Rev. B **86**, 155138 (2012).

[39] D. Lee, R. K. Behera, P. Wu, H. Xu, Y. L. Li, S. B. Sinnott, S. R. Phillpot, L. Q. Chen, and V. Gopalan, Mixed Bloch-Néel-Ising character of 180° ferroelectric domain walls, Phys. Rev. B **80**, 060102(R) (2009).

[40] R. K. Behera, Chan-Woo Lee, D. Lee, A. N. Morozovska, S. B. Sinnott, A. Asthagiri, V. Gopalan, and S. R. Phillpot, Structure and energetics of 180 ° domain walls in $PbTiO_3$ by density functional theory, J. Phys.: Condens. Matter **23**, 175902 (2011).

[41] W. Cao, Constructing Landau-Ginzburg-Devonshire type models for ferroelectric systems based on symmetry, Ferroelectrics **375**, 28 (2008).

[42] P. Marton, I. Rychetsky and J. Hlinka, Domain walls of ferroelectric $BaTiO_3$ within the Ginzburg-Landau-Devonshire phenomenological model, Phys. Rev. B **81**, 144125 (2010).

[43] I. I. Ivanchik, To macroscopic theory of ferroelectrics, Sov. Phys. Solid State **3**, 2705 (1962) [Fiz. Tverd. Tela **3**, 3731 (1961)].

[44] J. J. Wang, E. A. Eliseev, X. Q. Ma, P. P. Wu, A. N. Morozovska, and Long-Qing Chen, Strain effect on phase transitions of $BaTiO_3$ nanowires, Acta Mater. **59**, 7189 (2011).

[45] A. N. Morozovska, R. K. Vasudevan, P. Maksymovych, S. V. Kalinin, and E. A. Eliseev, Anisotropic conductivity of uncharged domain walls in $BiFeO_3$, Phys. Rev. B **86**, 085315 (2012).

[46] C.-L. Jia, V. Nagarajan, J.-Q. He, L. Houben, T. Zhao, R. Ramesh, K. Urban, and R. Waser, Unit-cell scale mapping of ferroelectricity and tetragonality in epitaxial ultrathin ferroelectric films, Nat. Mater. **6**, 64 (2007).

[47] C.-L. Jia, S.-B. Mi, K. Urban, I. Vrejoiu, M. Alexe, and D. Hesse, Atomic-scale study of electric dipoles near charged and uncharged domain walls in ferroelectric films, Nat. Mater. **7**, 57 (2008).

[48] C. L. Jia, S. B. Mi, K. Urban, I. Vrejoiu, M. Alexe, and D. Hesse, Effect of a Single Dislocation in a Heterostructure Layer on the Local Polarization of a Ferroelectric Layer, Phys. Rev. Lett. **102**, 117601 (2009).

[49] M. F. Chisholm, W. D. Luo, M. P. Oxley, S. T. Pantelides, and H. N. Lee, Atomic-Scale Compensation Phenomena at Polar Interfaces, Phys. Rev. Lett. **105**, 197602 (2010).

[50] C. T. Nelson, B. Winchester, Y. Zhang, S. J. Kim, A. Melville, C. Adamo, C. M. Folkman, S. H. Baek, C. B. Eom, D. G. Schlom, L. Q. Chen, and X. Q. Pan, Spontaneous Vortex Nanodomain Arrays at Ferroelectric Heterointerfaces, Nano Lett. **11**, 828 (2011).

[51] C. T. Nelson, P. Gao, J. R. Jokisaari, C. Heikes, C. Adamo, A. Melville, S. H. Baek, C. M. Folkman, B. Winchester, Y. J. Gu, Y. M. Liu, K. Zhang, E. G. Wang, J. Y. Li, L. Q. Chen, C. B. Eom, D. G. Schlom, and X. Q. Pan, Domain dynamics during ferroelectric switching, Science **334**, 968 (2011).

[52] S. Das, Y. L. Tang, Z. Hong, M. A. P. Goncalves, M. R. McCarter, C. Klewe, K. X. Nguyen, F. Gomez-Ortiz, P. Shafer, E. Arenholz, V. A. Stoica, S. L. Hsu, B. Wang, C. Ophus, J. F. Liu, C. T. Nelson, S. Saremi, B. Prasad, A. B. Mei, D. G. Schlom *et al.*, Observation of room-temperature polar skyrmions, Nature (London) **568**, 368 (2019).

[53] S. J. Pennycook, M. F. Chisholm, A. R. Lupini, M. Varela, A. Y. Borisevich, M. P. Oxley, W. D. Luo, K. van Benthem, S.-H. Oh, D. L. Sales, S. I. Molina, J. García-Barriocanal, C. Leon, J. Santamaría, S. N. Rashkeev, and S. T. Pantelides, Aberration-corrected scanning transmission electron microscopy: from atomic imaging and analysis to solving energy problems, Philos. Trans. R. Soc. A **367**, 3709 (2009).

[54] A. Y. Borisevich, E. A. Eliseev, A. N. Morozovska, C.-J. Cheng, J.-Y. Lin, Y. H. Chu, D. Kan, I. Takeuchi, V. Nagarajan, and S. V. Kalinin, Atomic-scale evolution of modulated phases at the ferroelectricantiferroelectric morphotropic phase boundary controlled by flexoelectric interaction, Nat. Commun. **3**, 775 (2012).

[55] A. Y. Borisevich, A. R. Lupini, J. He, E. A. Eliseev, A. N. Morozovska, G. S. Svechnikov, P. Yu, Y.-H. Chu, R. Ramesh, S. T. Pantelides, S. V. Kalinin, and S. J. Pennycook, Interface dipole between two metallic oxides caused by localized oxygen vacancies, Phys. Rev. B **86**, 140102(R) (2012).

[56] A. Y. Borisevich, A. N. Morozovska, Y.-M. Kim, D. Leonard, M. P. Oxley, M. D. Biegalski, E. A. Eliseev, and S. V. Kalinin, Exploring Mesoscopic Physics of Vacancy-Ordered Systems through Atomic Scale Observations of Topological Defects, Phys. Rev. Lett. **109**, 065702 (2012).

[57] Q. Li, C. T. Nelson, S.-L. Hsu, A. R. Damodaran, L.-L. Li, A. K. Yadav, M. McCarter, L. W. Martin, R. Ramesh, and S. V. Kalinin, Quantification of flexoelectricity in $PbTiO_3/SrTiO_3$ superlattice polar vortices using machine learning and phase-field modeling, Nat. Commun. **8**, 1468 (2017).

[58] R. K. Vasudevan, K. P. Kelley, E. Eliseev, S. Jesse, H. Funakubo, A. Morozovska, and S. V. Kalinin, Bayesian inference in band excitation Scanning Probe Microscopy for optimal dynamic model selection in imaging, J. Appl. Phys. **128**, 054105 (2020).

[59] M. Ziatdinov, C. Nelson, X. Zhang, R. Vasudevan, E. Eliseev, A. N. Morozovska, I. Takeuchi, and S. V. Kalinin, Causal analysis of competing atomistic mechanisms in ferroelectric materials from high-resolution scanning transmission electron microscopy data, npj Comput. Mater. **6**, 127 (2020).

[60] L. D. Landau and I. M. Khalatnikov, On the anomalous absorption of sound near a second order phase transition point, Dokl. Akad. Nauk SSSR **96**, 469 (1954).

[61] R. Kretschmer and K. Binder, Surface effects on phase transition in ferroelectrics and dipolar magnets, Phys. Rev. B **20**, 1065 (1979).

[62] See Supplemental Material at http://link.aps.org/supplemental/10.1103/PhysRevMaterials.4.114410 for calculation details.

[63] A. K. Tagantsev, M. Landivar, E. Colla, and N. Setter, Identification of passive layer in ferroelectric thin films from their switching parameters, J. Appl. Phys. **78**, 2623 (1995).

[64] E. Fermi, J. Pasta, and S. Ulam, Studies of Nonlinear Problems, Document LA-1940, Los Alamos National Laboratory, 1955.

[65] T. Dauxois, Fermi, Pasta, Ulam, and a mysterious lady, Phys. Today **61**(1), 55 (2008).

[66] http://energy.gov/downloads/doe-public-access-plan.